Electronic Supplementary Material (ESI) for Inorganic Chemistry Frontiers.
This journal is © the Partner Organisations 2019

SUPPORTING INFORMATION

Near-infrared emissive Er(III) and Yb(III) molecular nanomagnets in metal–organic chains functionalized by octacyanidometallates(IV)

Robert Jankowski,[a] Jakub J. Zakrzewski,[a] Olga Surma,[a] Shin-ichi Ohkoshi,[b] Szymon Chorazy,*[a],[b] and Barbara Sieklucka*[a]

[a] Faculty of Chemistry, Jagiellonian University, Gronostajowa 2, 30-387 Kraków, Poland. [b] Department of Chemistry, School of Science, The University of Tokyo, 7-3-1 Hongo, Bunkyo-ku, Tokyo 113-0033, Japan.

*Corresponding authors: chorazy@chemia.uj.edu.pl; barbara.sieklucka@uj.edu.pl

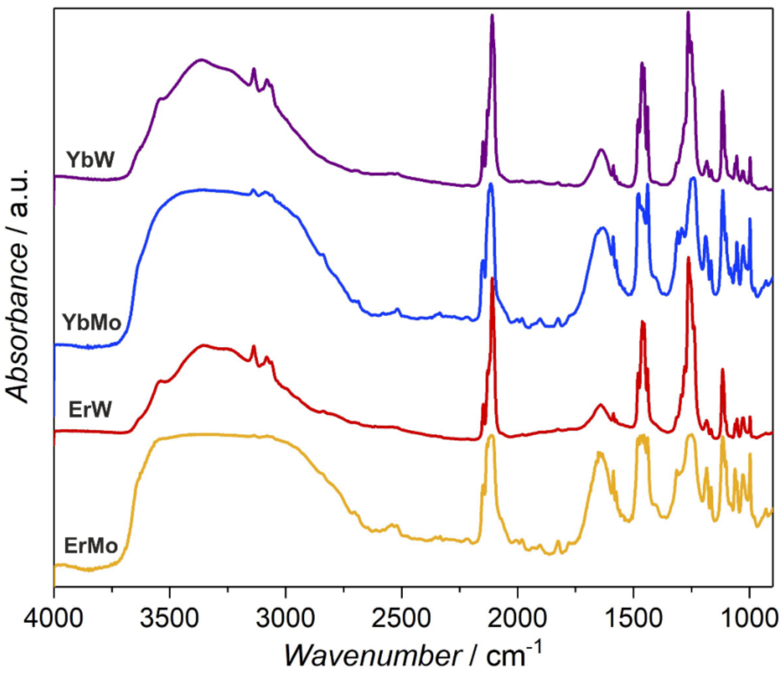

Figure S1. Infrared absorption spectra of the crystalline samples of **ErMo**, **ErW**, **YbMo** and **YbW**, collected in the 4000–900 cm^{-1} range.

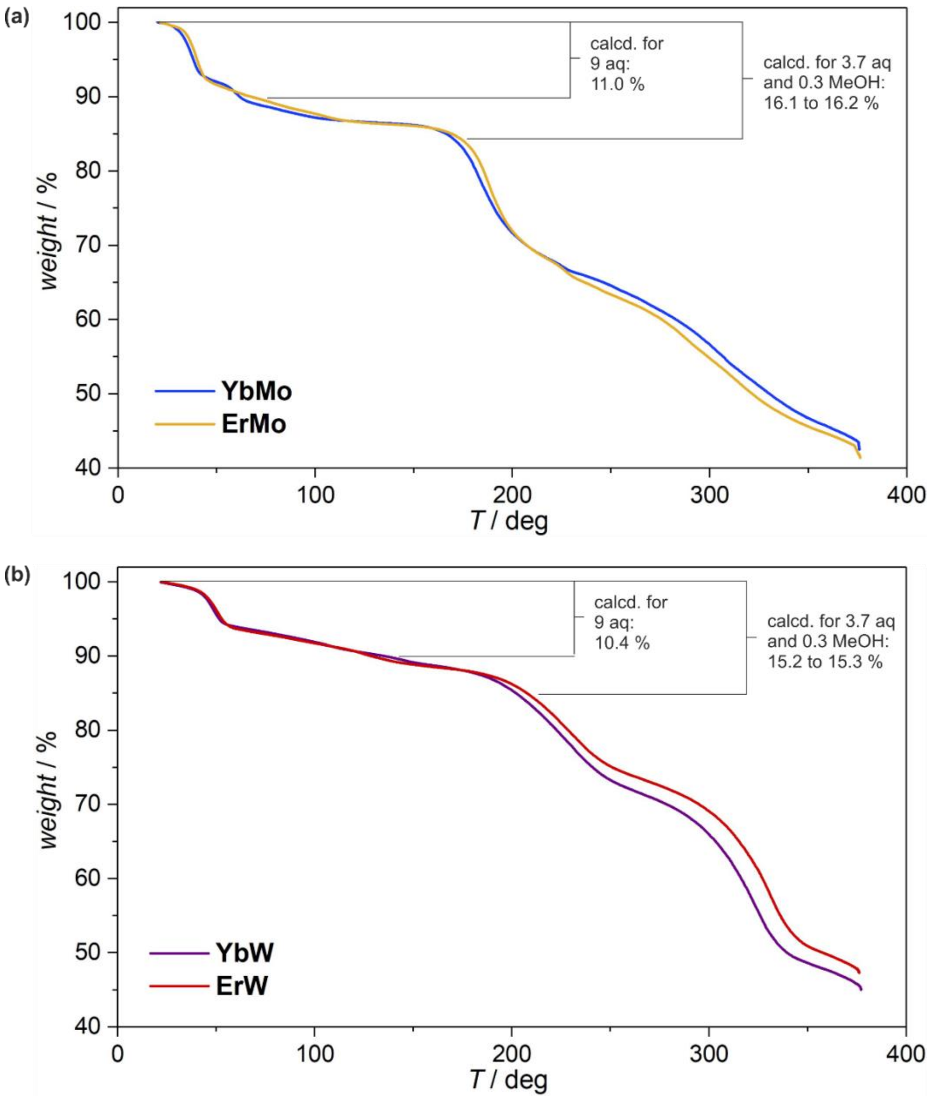

Figure S2. Thermogravimetric curves collected in the temperature range of 20–375 °C for **ErMo**, **ErW** (*a*) and **YbMo**, **YbW** (*b*). The steps related to the loss of solvent molecules are depicted. The experiments were conducted under an air atmosphere with the heating rate of 1 °C per minute.

Comment to Figure S2

Upon heating under an air atmosphere, the powder samples of the reported compounds exhibit abrupt decrease of the sample mass in the range from room temperature to ca. 50 °C. It is followed by the gradual, smaller decrease of the mass in the broad temperature range up to ca. 180 °C with the distinguishable tiny step below 100 °C, visible especially for **YbMo** and **ErMo**. The related decreases of the sample mass can be reasonably correlated with the amount of solvent molecules determined by the CHN elemental analysis (see Experimental section). The first step below 50 °C together with the subsequent decrease below ca. 100 °C may be assigned to the removal of water of crystallization in the amount found from CHN elemental analysis. The further decrease of the mass up to ca. 180 °C has to be ascribed to the removal of coordinated solvent molecules. However, there is no clear plateau after full desolvation which can be interpreted in terms of the resulting fast destabilization of the crystal structure and further removal of terminal cyanides accompanied by the overall decomposition of compounds.

Table S1. Crystal data and structure refinement for **ErMo**, **ErW**, **YbMo** and **YbW**.

Compound		**ErMo**	**ErW**	**YbMo**	**YbW**
formula		$Er_2Mo_2C_{108.6}H_{128}N_{26}O_{35.4}P_4$	$Er_2W_2C_{108.6}H_{124}N_{26}O_{35.4}P_4$	$Yb_2Mo_2C_{108.6}H_{128}N_{26}O_{35.4}P_4$	$Yb_2W_2C_{108.6}H_{124}N_{26}O_{35.4}P_4$
formula weight [$g\cdot mol^{-1}$]		3014.24	3186.03	3025.8	3197.59
T [K]		100(2)			
λ [Å]		0.71073			
crystal system		monoclinic			
space group		$P\ 2_1/c$			
unit cell	$\boldsymbol{a}$ [Å]	11.1793(3)	11.1835(5)	11.1828(4)	11.1666(3)
	$\boldsymbol{b}$ [Å]	13.1976(4)	13.2011(5)	13.1725(5)	13.1043(4)
	$\boldsymbol{c}$ [Å]	43.0696(13)	43.0944(18)	43.0580(16)	43.0681(13)
	β [deg]	91.9180(10)	91.9000(10)	91.9510(10)	92.0600(10)
V [$Å^3$]		6350.9(3)	6358.7(5)	6339.0(4)	6298.1(3)
Z		2	2	2	2
calculated density [$g\cdot cm^{-3}$]		1.576	1.664	1.585	1.686
absorption coefficient [cm^{-1}]		1.638	3.247	1.793	3.430
F(000)		3050	3170	3058	3178
crystal size [mm × mm × mm]		0.45 × 0.39 × 0.16	0.14 × 0.13 × 0.10	0.25 × 0.22 × 0.18	0.14 × 0.07 × 0.04
crystal type		red block	black block	red block	black block
Θ range [deg]		2.423–27.103	2.546–26.372	2.390–27.103	2.397–27.103
limiting indices		$-14 < h < 14$ $-16 < k < 16$ $-55 < l < 55$	$-13 < h < 13$ $-15 < k < 16$ $-53 < l < 53$	$-14 < h < 14$ $-16 < k < 16$ $-55 < l < 55$	$-14 < h < 14$ $-16 < k < 16$ $-55 < l < 55$
collected reflections		69956	36240	70289	68360
unique reflections		13997	12982	13981	13886
R_{int}		0.0541	0.0651	0.0627	0.1121
completeness		0.999	0.998	0.999	0.999
max. and min. transmission		0.526 and 0.779	0.659 and 0.737	0.663 and 0.738	0.645 and 0.875
data/restraints/ parameters		13997/27/865	12982/ 71/ 850	13981/27/865	13886/99/850
GOF on F^2		1.286	1.165	1.181	1.402
final R indices		$R_1 = 0.0531[I>2\sigma(I)]$ $wR_2 = 0.1038$ (all data)	$R_1 = 0.0589[I>2\sigma(I)]$ $wR_2 = 0.1136$ (all data)	$R_1 = 0.0487[I>2\sigma(I)]$ $wR_2 = 0.0934$ (all data)	$R_1 = 0.0944[I>2\sigma(I)]$ $wR_2 = 0.1708$ (all data)
largest diff peak/hole		1.883/-2.288 $e\cdot Å^{-3}$	2.743/ -2.527 $e\cdot Å^{-3}$	1.355/-1.758 $e\cdot Å^{-3}$	3.047/-5.538 $e\cdot Å^{-3}$

Table S2. Detailed structure parameters of Ln^{3+} complexes in the crystal structures of **ErMo** and **YbMo**.

Parameter	**ErMo**	**YbMo**
Ln1–O1	2.300(3) Å	2.280(3) Å
Ln1–O2	2.368(4) Å	2.356(3) Å
Ln1–O3	2.362(3) Å	2.343(3) Å
Ln1–O4	2.363(3) Å	2.353(3) Å
Ln1–O5	2.320(3) Å	2.300(3) Å
Ln1–O6	2.305(3) Å	2.290(3) Å
Ln1–O7/O8	2.347(3) Å	2.325(3) Å
Ln1–N1	2.412(4) Å	2.390(4) Å
O1–Ln1–O2	75.97(13)°	75.71(12)°
O1–Ln1–O3	107.47(13)°	106.89(12)°
O1–Ln1–O4	69.87(12)°	69.69(11)°
O1–Ln1–O5	139.36(12)°	139.39(11)°
O1–Ln1–O6	145.24(13)°	145.48(12)°
O1–Ln1–O7/O8	87.00(13)°	87.31(12)°
O1–Ln1–N1	74.12(13)°	74.23(12)°
O2–Ln1–O3	70.92(12)°	71.11(11)°
O2–Ln1–O4	121.29(13)°	121.52(12)°
O2–Ln1–O5	137.90(12)°	138.01(11)°
O2–Ln1–O6	80.24(13)°	80.28(12)°
O2–Ln1–O7/O8	144.84(12)°	144.74(11)°
O2–Ln1–N1	74.01(13)°	73.88(12)°
O3–Ln1–O4	75.74(12)°	75.78(11)°
O3–Ln1–O5	75.29(12)°	75.35(12)°
O3–Ln1–O6	87.85(13)°	87.96(12)°
O3–Ln1–O7/O8	144.20(12)°	144.10(11)°
O3–Ln1–N1	143.11(13)°	143.28(12)°
O4–Ln1–O5	71.85(11)°	71.88(11)°
O4–Ln1–O6	144.89(12)°	144.83(11)°
O4–Ln1–O7/O8	79.20(12)°	78.89(11)°
O4–Ln1–N1	134.39(12)°	134.04(12)°
O5–Ln1–O6	74.05(12)°	73.93(11)°
O5–Ln1–O7/O8	72.84(12)°	72.83(11)°
O5–Ln1–N1	128.19(13)°	128.28(12)°
O6–Ln1–O7/O8	98.59(13)°	98.71(12)°
O6–Ln1–N1	75.20(13)°	75.51(12)°
O7/O8–Ln1–N1	71.80(13)°	71.83(12)°

Table S3. Detailed structure parameters of Ln^{3+} complexes in the crystal structures of **ErW** and **YbW**.

Parameter	ErW	YbW
Ln1–O1	2.301(6) Å	2.274(9) Å
Ln1–O2	2.374(5) Å	2.366(9) Å
Ln1–O3	2.367(5) Å	2.340(8) Å
Ln1–O4	2.369(5) Å	2.357(8) Å
Ln1–O5	2.323(5) Å	2.293(8) Å
Ln1–O6	2.299(5) Å	2.266(8) Å
Ln1–O7/O8	2.346(5) Å	2.334(8) Å
Ln1–N1	2.414(7) Å	2.391(10) Å
O1–Ln1–O2	76.5(2)°	76.0(3)°
O1–Ln1–O3	107.4(2)°	107.2(3)°
O1–Ln1–O4	69.08(19)°	70.2(3)°
O1–Ln1–O5	138.74(19)°	139.3(3)°
O1–Ln1–O6	146.3(2)°	145.8(3)°
O1–Ln1–O7/O8	86.6(2)°	86.6(3)°
O1–Ln1–N1	74.6(2)°	74.2(3)°
O2–Ln1–O3	71.02(19)°	70.8(3)°
O2–Ln1–O4	121.5(2)°	121.7(3)°
O2–Ln1–O5	137.82(19)°	137.8(3)°
O2–Ln1–O6	80.5(2)°	80.3(3)°
O2–Ln1–O7/O8	144.45(19)°	144.9(3)°
O2–Ln1–N1	73.7(2)°	74.1(3)°
O3–Ln1–O4	76.02(19)°	75.7(3)°
O3–Ln1–O5	75.16(19)°	75.4(3)°
O3–Ln1–O6	87.7(2)°	87.6(3)°
O3–Ln1–O7/O8	144.50(18)°	144.2(3)°
O3–Ln1–N1	142.9(2)°	143.2(3)°
O4–Ln1–O5	71.94(18)°	71.4(3)°
O4–Ln1–O6	144.63(19)°	144.0(3)°
O4–Ln1–O7/O8	79.21(19)°	78.6(3)°
O4–Ln1–N1	134.2(2)°	134.5(3)°
O5–Ln1–O6	73.62(18)°	73.6(3)°
O5–Ln1–O7/O8	73.21(19)°	73.1(3)°
O5–Ln1–N1	128.38(19)°	128.1(3)°
O6–Ln1–O7/O8	98.4(2)°	99.2(3)°
O6–Ln1–N1	75.5(2)°	75.7(3)°
O7/O8–Ln1–N1	71.7(2)°	71.8(3)°

Table S4. Detailed structure parameters of $[Mo(CN)_8]^{4-}$ units in the crystal structures of **ErMo** and **YbMo**.

Parameter	ErMo	YbMo
Mo1–C1	2.143(5) Å	2.149(4) Å
Mo1–C2	2.166(5) Å	2.167(5) Å
Mo1–C3	2.169(5) Å	2.167(5) Å
Mo1–C4	2.157(5) Å	2.160(5) Å
Mo1–C5	2.148(5) Å	2.145(5) Å
Mo1–C6	2.148(5) Å	2.152(5) Å
Mo1–C7	2.159(5) Å	2.166(5) Å
Mo1–C8	2.166(5) Å	2.168(5) Å
C1–Mo1–C2	71.90(18)°	71.63(17)°
C1–Mo1–C3	142.12(18)°	142.02(17)°
C1–Mo1–C4	140.85(18)°	140.96(17)°
C1–Mo1–C5	79.38(18)°	79.41(17)°
C1–Mo1–C6	75.92(18)°	76.09(16)°
C1–Mo1–C7	73.03(18)°	73.21(16)°
C1–Mo1–C8	114.60(18)°	114.56(17)°
C2–Mo1–C3	77.20(19)°	77.36(18)°
C2–Mo1–C4	146.26(19)°	146.47(18)°
C2–Mo1–C5	80.96(19)°	81.03(18)°
C2–Mo1–C6	140.65(19)°	140.73(17)°
C2–Mo1–C7	114.04(18)°	114.12(17)°
C2–Mo1–C8	74.01(19)°	73.99(18)°
C3–Mo1–C4	74.57(19)°	74.54(18)°
C3–Mo1–C5	74.54(18)°	74.52(17)°
C3–Mo1–C6	119.39(19)°	119.48(18)°
C3–Mo1–C7	141.51(18)°	141.46(17)°
C3–Mo1–C8	76.03(18)°	75.96(17)°
C4–Mo1–C5	108.48(19)°	108.25(17)°
C4–Mo1–C6	71.08(18)°	70.84(17)°
C4–Mo1–C7	79.14(18)°	79.09(17)°
C4–Mo1–C8	81.52(19)°	81.71(18)°
C5–Mo1–C6	71.29(19)°	71.48(18)°
C5–Mo1–C7	141.56(18)°	141.53(18)°
C5–Mo1–C8	144.78(19)°	144.71(18)°
C6–Mo1–C7	76.35(18)°	76.02(18)°
C6–Mo1–C8	141.79(18)°	141.64(17)°
C7–Mo1–C8	72.66(18)°	72.81(17)°

Table S5. Detailed structure parameters of $[WCN)_8]^{4-}$ units in the crystal structures of **ErW** and **YbW**.

Parameter	ErW	YbW
W1–C1	2.149(8) Å	2.149(10) Å
W1–C2	2.179(9) Å	2.172(13) Å
W1–C3	2.159(9) Å	2.161(12) Å
W1–C4	2.151(8) Å	2.157(12) Å
W1–C5	2.145(9) Å	2.152(13) Å
W1–C6	2.141(8) Å	2.148(12) Å
W1–C7	2.157(8) Å	2.151(11) Å
W1–C8	2.169(9) Å	2.178(14) Å
C1–W1–C2	72.0(3)°	72.0(4)°
C1–W1–C3	142.2(3)°	142.0(4)°
C1–W1–C4	141.1(3)°	140.9(4)°
C1–W1–C5	79.1(3)°	79.1(4)°
C1–W1–C6	75.7(3)°	75.6(4)°
C1–W1–C7	73.1(3)°	73.4(4)°
C1–W1–C8	114.5(3)°	114.1(4)°
C2–W1–C3	77.2(3)°	76.9(4)°
C2–W1–C4	145.9(3)°	146.3(4)°
C2–W1–C5	81.1(3)°	81.1(5)°
C2–W1–C6	140.8(3)°	140.4(4)°
C2–W1–C7	113.8(3)°	114.4(4)°
C2–W1–C8	73.9(3)°	74.1(5)°
C3–W1–C4	74.4(3)°	74.7(4)°
C3–W1–C5	74.9(3)°	74.9(4)°
C3–W1–C6	119.6(3)°	119.8(4)°
C3–W1–C7	141.3(3)°	141.2(4)°
C3–W1–C8	76.2(3)°	76.6(4)°
C4–W1–C5	108.7(3)°	108.3(4)°
C4–W1–C6	71.5(3)°	71.3(4)°
C4–W1–C7	79.3(3)°	78.9(4)°
C4–W1–C8	81.3(3)°	81.8(4)°
C5–W1–C6	71.2(3)°	70.9(5)°
C5–W1–C7	141.5(3)°	141.4(4)°
C5–W1–C8	145.2(3)°	145.6(5)°
C6–W1–C7	76.4(3)°	76.2(4)°
C6–W1–C8	141.6(3)°	141.6(5)°
C7–W1–C8	72.3(3)°	72.0(4)°

Table S6. Results of Continuous Shape Measure Analysis for lanthanide(III) complexes in the crystal structures of **ErMo**, **ErW**, **YbMo** and **YbW**.

Compound	CSM parameters*			Geometry
	SAPR–8	TDD–8	BTPR–8	
ErMo	1.283	0.765	1.290	TDD–8
ErW	1.315	0.796	1.282	TDD-8
YbMo	1.307	0.731	1.322	TDD-8
YbW	1.252	0.772	1.305	TDD-8

* CSM parameters:
CSM SAPR–8= the parameter related to the square antiprism geometry (D_{4d} symmetry)
CSM TDD–8= the parameter related to the triangular dodecahedron geometry (D_{2d} symmetry)
CSM BTPR–8 = the parameter related to the biaugmented trigonal prism geometry (C_{2v} symmetry)
CSM = 0 for the ideal geometry and the increase of CSM parameter represents the increasing distortion from the ideal polyhedron.

References: (*a*) M. Llunell, D. Casanova, J. Cirera, J. Bofill, P. Alemany, S. Alvarez, M. Pinsky and D. Avnir, *SHAPE v. 2.1. Program for the Calculation of Continuous Shape Measures of Polygonal and Polyhedral Molecular Fragments,* University of Barcelona: Barcelona, Spain, 2013; (*b*) D. Casanova, J. Cirera, M. Llunell, P. Alemany, D. Avnir and S. Alvarez, *J. Am. Chem. Soc.*, 2004, **126**, 1755.

Table S7. Results of Continuous Shape Measure Analysis for $[M^{IV}(CN)_8]^{4-}$ (M^{IV} = Mo, W) units in the crystal structures of **ErMo**, **ErW**, **YbMo** and **YbW**.

Compound	CSM parameters*			Geometry
	SAPR–8	TDD–8	BTPR–8	
ErMo	0.285	2.077	1.721	SAPR–8
ErW	0.282	2.105	1.705	SAPR–8
YbMo	0.293	2.064	1.692	SAPR–8
YbW	0.300	2.014	1.698	SAPR–8

* CSM parameters:
CSM SAPR–8= the parameter related to the square antiprism geometry (D_{4d} symmetry)
CSM TDD–8= the parameter related to the triangular dodecahedron geometry (D_{2d} symmetry)
CSM BTPR–8 = the parameter related to the biaugmented trigonal prism geometry (C_{2v} symmetry)
CSM = 0 for the ideal geometry and the increase of CSM parameter represents the increasing distortion from the ideal polyhedron.

References: (*a*) M. Llunell, D. Casanova, J. Cirera, J. Bofill, P. Alemany, S. Alvarez, M. Pinsky and D. Avnir, *SHAPE v. 2.1. Program for the Calculation of Continuous Shape Measures of Polygonal and Polyhedral Molecular Fragments,* University of Barcelona: Barcelona, Spain, 2013; (*b*) D. Casanova, J. Cirera, M. Llunell, P. Alemany, D. Avnir and S. Alvarez, *J. Am. Chem. Soc.*, 2004, **126**, 1755.

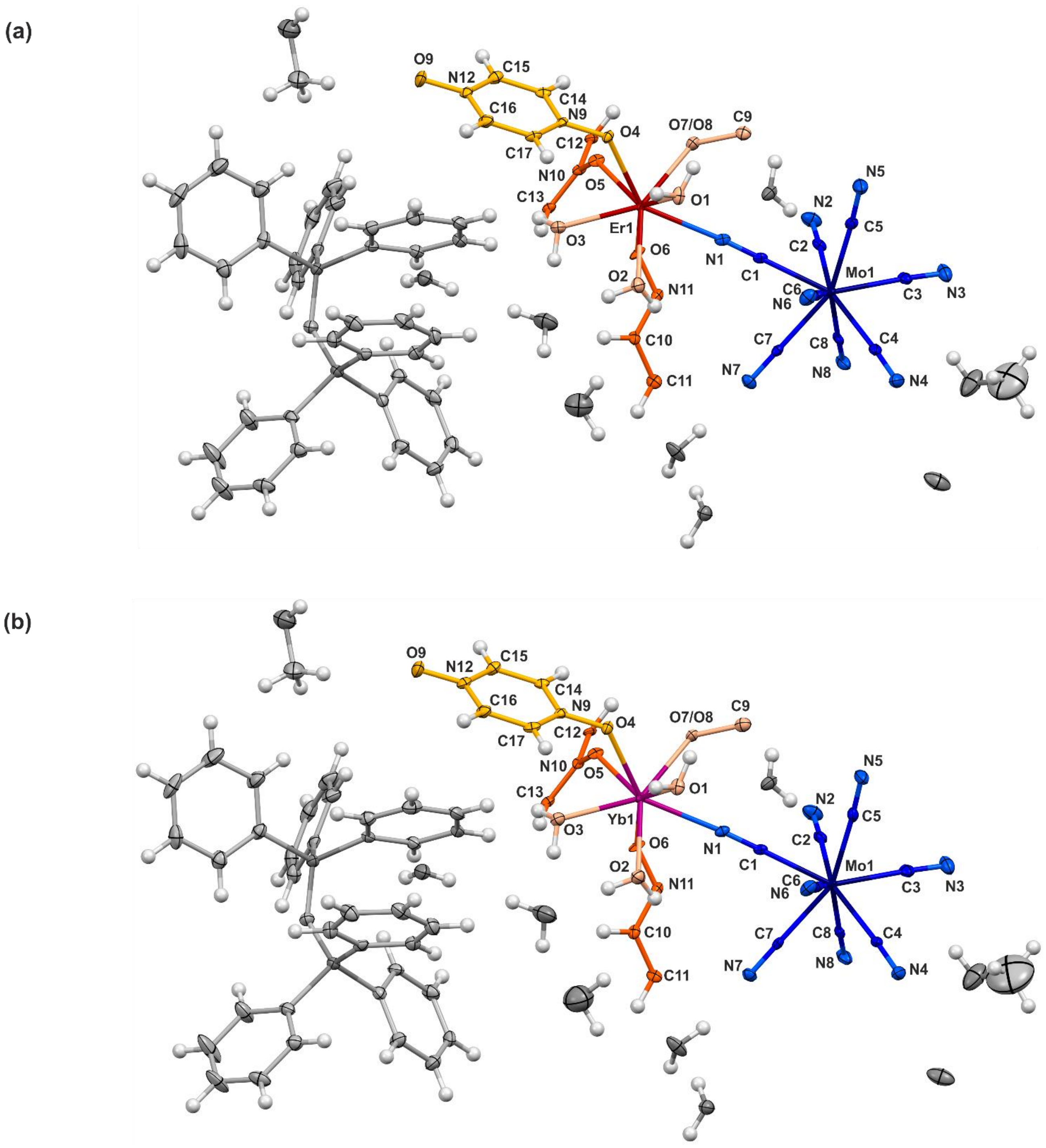

Figure S3. Comparison of the asymmetric units of **ErMo** (*a*) and **YbMo** (*b*) with the atoms labelling schemes. Thermal ellipsoids are presented at the 50% probability level. The related bond lengths and angles are collected in Tables S1 and S3. Hydrogen atoms were drawn as fixed-sized spheres with the 0.2 Å radius.

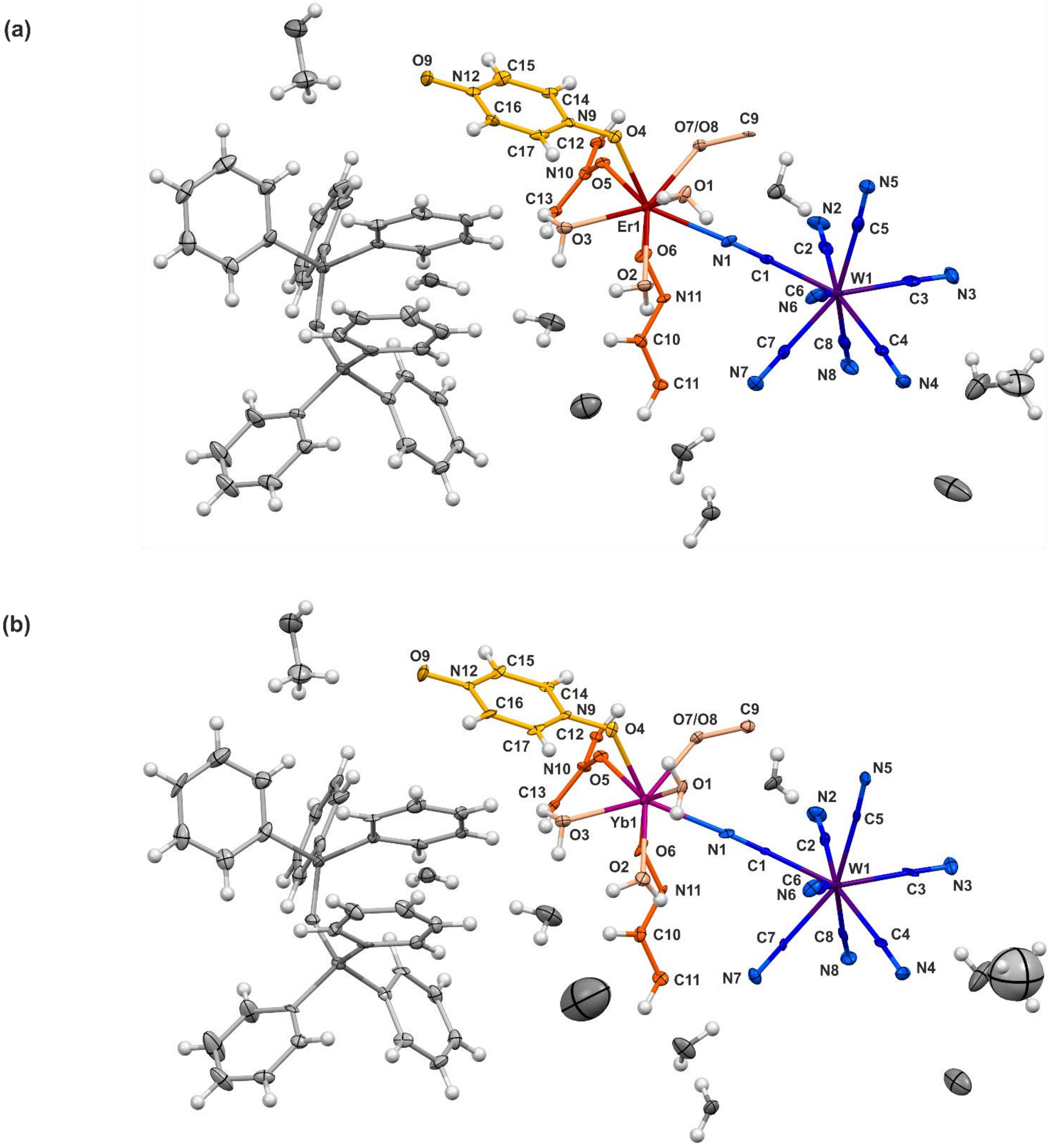

Figure S4. Comparison of the asymmetric units of **ErW** (*a*) and **YbW** (*b*) with the atoms labelling schemes. Thermal ellipsoids are presented at the 50% probability level. The related bond lengths and angles are collected in Tables S2 and S4. Hydrogen atoms were drawn as fixed-sized spheres with the 0.2 Å radius.

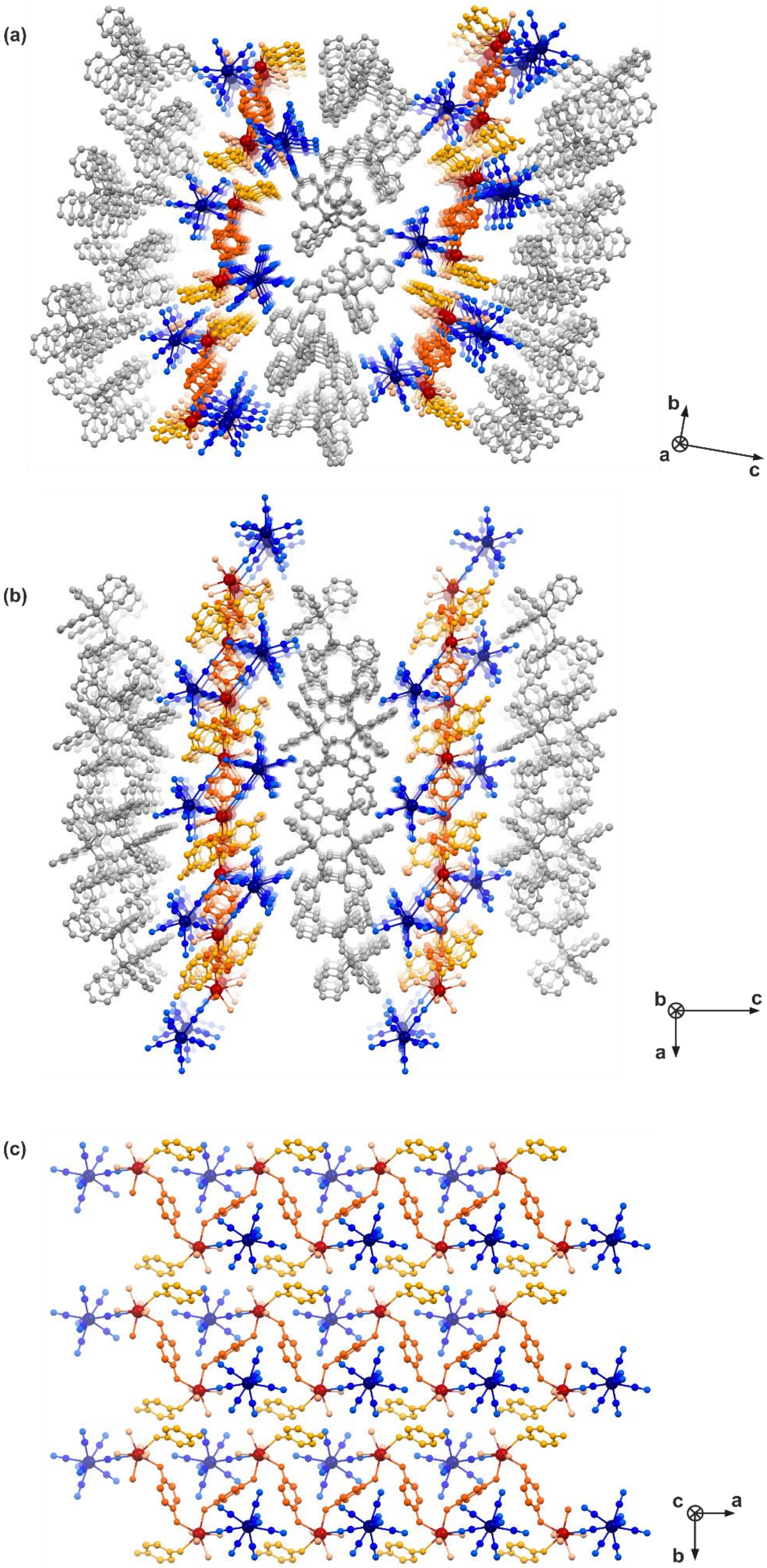

Figure S5. The views of the supramolecular networks in **ErMo** shown along the crystallographic ***a*** axis (*a*), ***b*** axis (*b*) and ***c*** axis (*c*). Crystallization solvent molecules and organic cations in *(c)* were omitted for clarity.

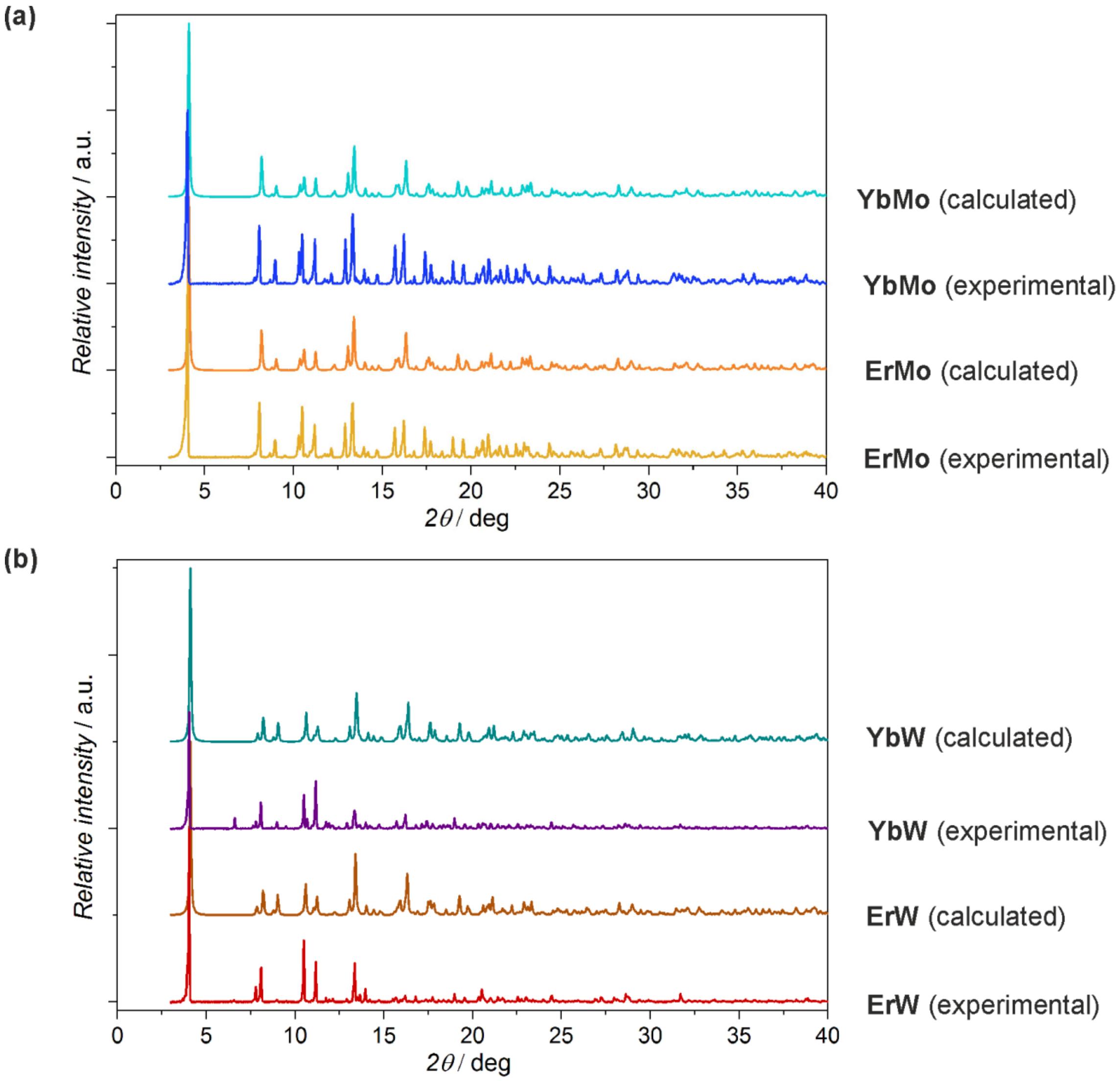

Figure S6. Experimental powder X-ray diffraction (PXRD) patterns of **ErMo**, **YbMo** (*a*), **ErW** and **YbW** (*b*). The PXRD patterns calculated from the structural models of all compounds obtained within the single crystal X-ray diffraction structural analyses were presented for comparison.

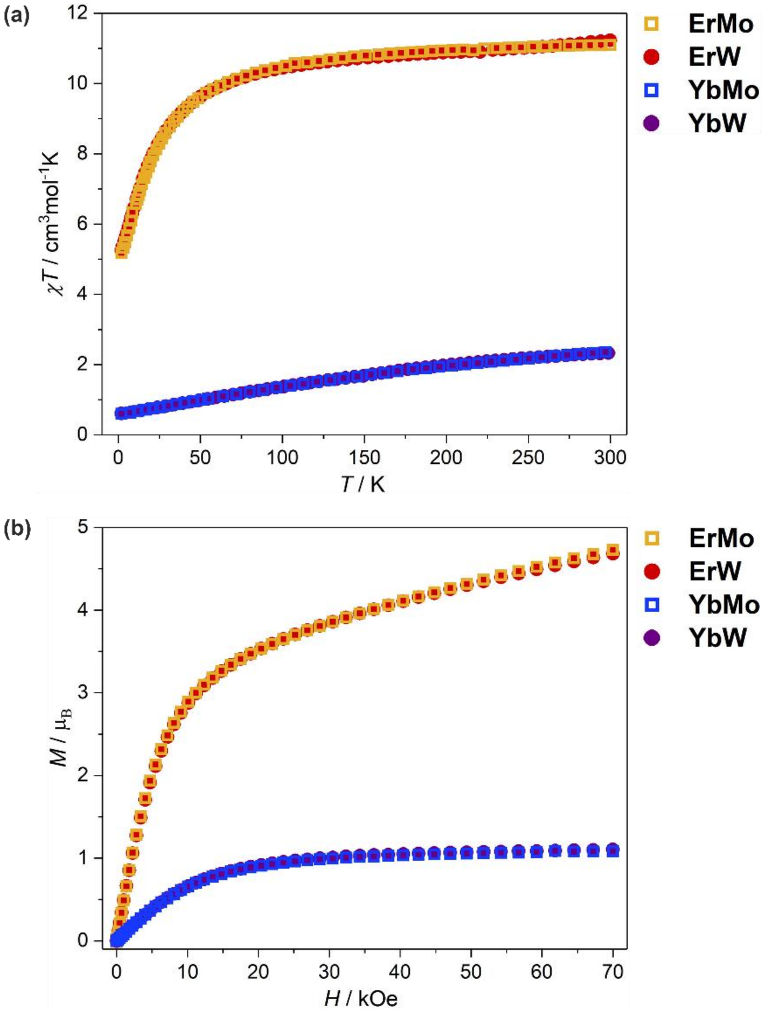

Figure S7. Static (*dc*) magnetic properties of **ErMo**, **ErW**, **YbMo** and **YbW**: (*a*) temperature dependences of the χT product at H_{dc} = 1000 Oe and (*b*) the field dependences of molar magnetization, M at T = 1.8 K.

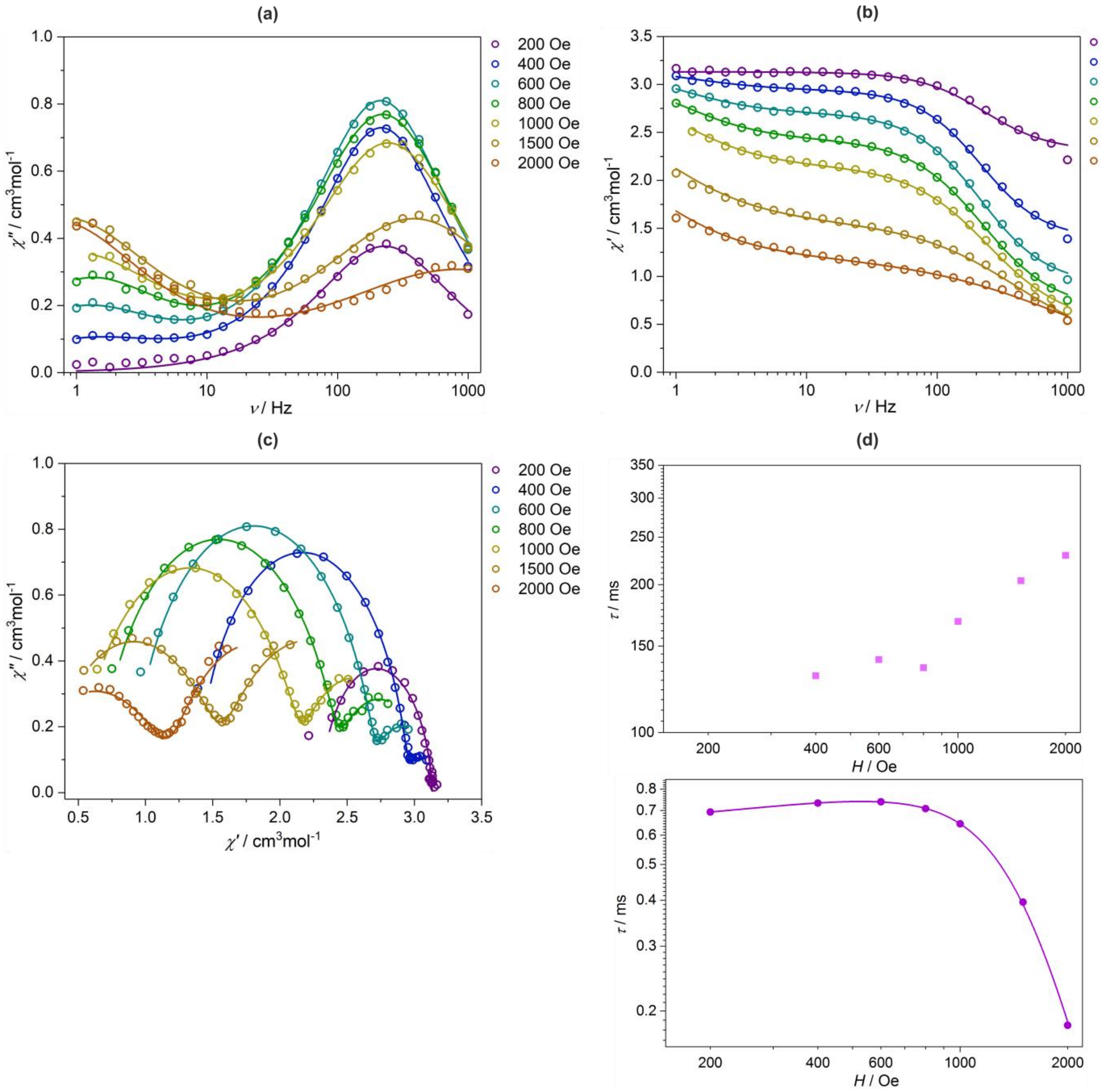

Figure S8. Complete magnetic-field-variable alternate-current (*ac*) magnetic susceptibility characteristics of **ErMo** at T = 1.8 K, under H_{ac} = 1 Oe, and their analysis: frequency dependences of the out-of-phase susceptibility, χ'' (*a*), and the in-phase susceptibility, χ' (*b*) at various indicated *dc* external magnetic fields, together with the related Argand plots (*c*), and the resulting field dependence of the relaxation time, τ, divided into two parts related to the slower (top) and faster relaxation processes (bottom) (*d*). Both field and relaxation time were presented in (*d*) in the logarithmic scale. Coloured solid curves in (*a*), (*b*), and (*c*) represent the best fits following the generalized Debye model for two relaxation processes (see comment on Page S22). The solid line in (*d*, bottom) shows the best fit of the faster relaxation process taking into account quantum tunnelling of magnetization and the direct process in the range of 200–2000 Oe. The τ versus H_{dc} dependence was then fitted using the equation (I):

$$\tau^{-1} = ATH^4 + \frac{a(1+c^2H^2)}{(1+bH^2)} \qquad \text{(I)}$$

where the first term represented by the A parameter is related to the field-induced direct process while the second term represented by three parameters (a, b and c) shows the contribution from QTM. The best-fit parameters were gathered in Table 2. Slow relaxation process represented by the relaxation times presented in (*d*, top) can be ascribed to the influence of weak magnetic dipole–magnetic dipole interactions between Er(III) centers as it becomes more significant and slows down with the increasing magnetic field. We found similar behaviour in cyanido-bridged {DyCo} SMMs (S. Chorazy, J. J. Zakrzewski, M. Reczyński, K. Nakabayashi, S. Ohkoshi and B. Sieklucka, *J. Mater. Chem. C*, 2019, **7**, 4164).

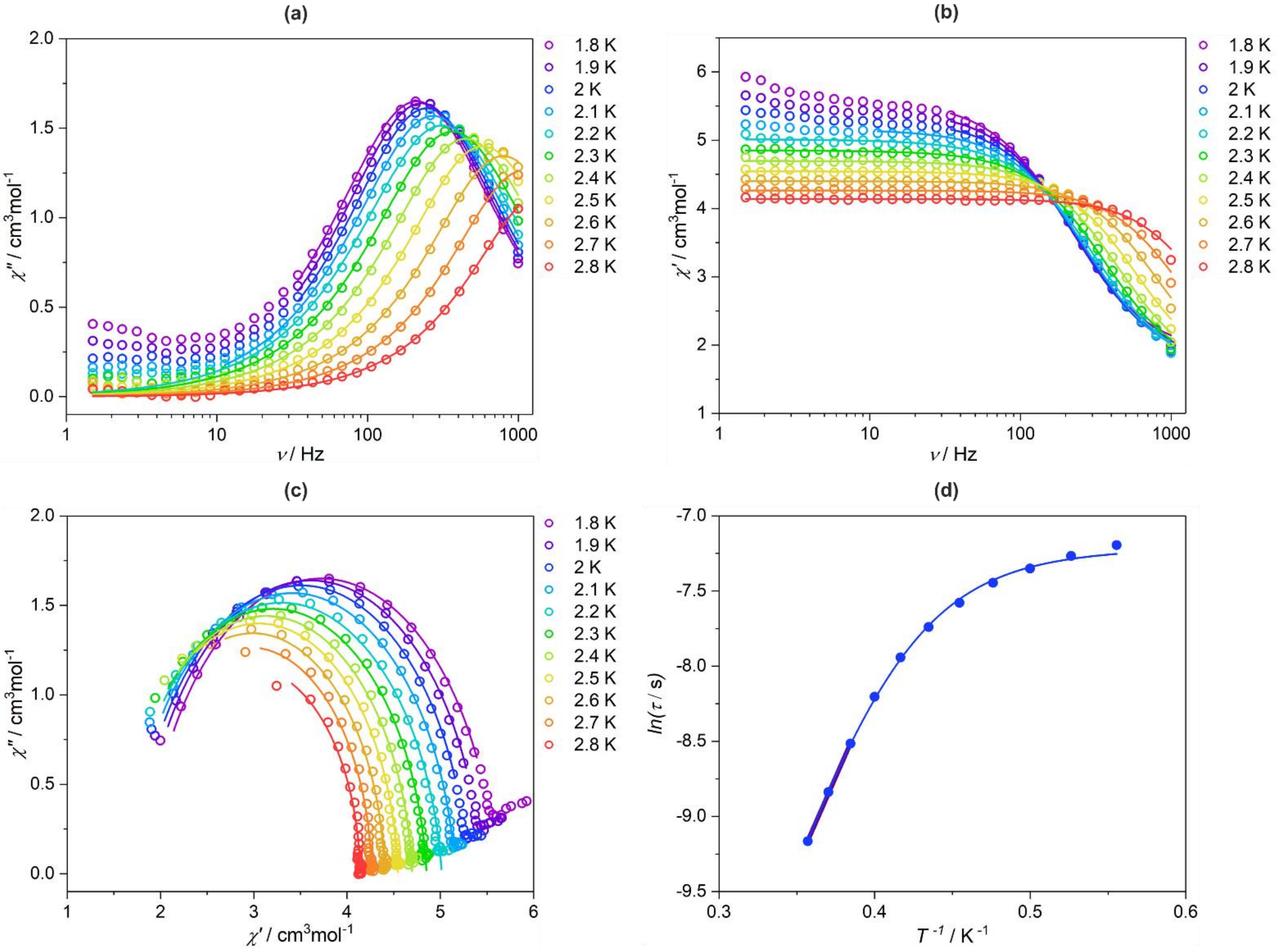

Figure S9. Complete temperature-variable alternate-current (*ac*) magnetic susceptibility characteristics of **ErMo** under H_{ac} = 1 Oe, H_{dc} = 600 Oe, and their analysis: frequency dependences of the out-of-phase susceptibility, χ'' (*a*), and the in-phase susceptibility, χ' (*b*) at various indicated temperatures, together with the related Argand plots (*c*), and the temperature dependence of the relaxation time, τ (*d*). Coloured solid curves in (*a*), (*b*), and (*c*) represent the best fits using the generalized Debye model for a single relaxation process (see comment on Page S22) . The solid deep blue line in (*d*) represents the linear fitting following the Arrhenius law ($\ln\tau = \ln\tau_0 - (U_{eff}/k_B)\cdot T^{-1}$) in the range of 2.6–2.8 K. The best-fit parameters are U_{eff}/k_B = 24(1) K with $\tau_0 = 2.3(4)\cdot 10^{-8}$ s. The blue solid line in (*d*) shows the best fit of the full temperature-dependence of the relaxation time in the range of 1.8–2.8 K. The Orbach and Raman relaxation processes were taken into the account together with the direct process and quantum tunnelling of magnetization (QTM), both extracted from the field-dependence of the relaxation time. Therefore, we followed the equation (II):

$$\tau^{-1} = \tau_0^{-1}\exp(-U_{eff}/k_B T) + B_{Raman}T^n + \tau_{QTM}^{-1} + AH^4T \qquad \text{(II)}$$

where the first term with two fitting parameters (τ_0, U_{eff}/k_B) represents the Orbach thermal relaxation, the second term indicates the Raman process, the third term shows the contribution from the QTM effect while the last originates from the direct process. The best-fit parameters were gathered in Table 2.

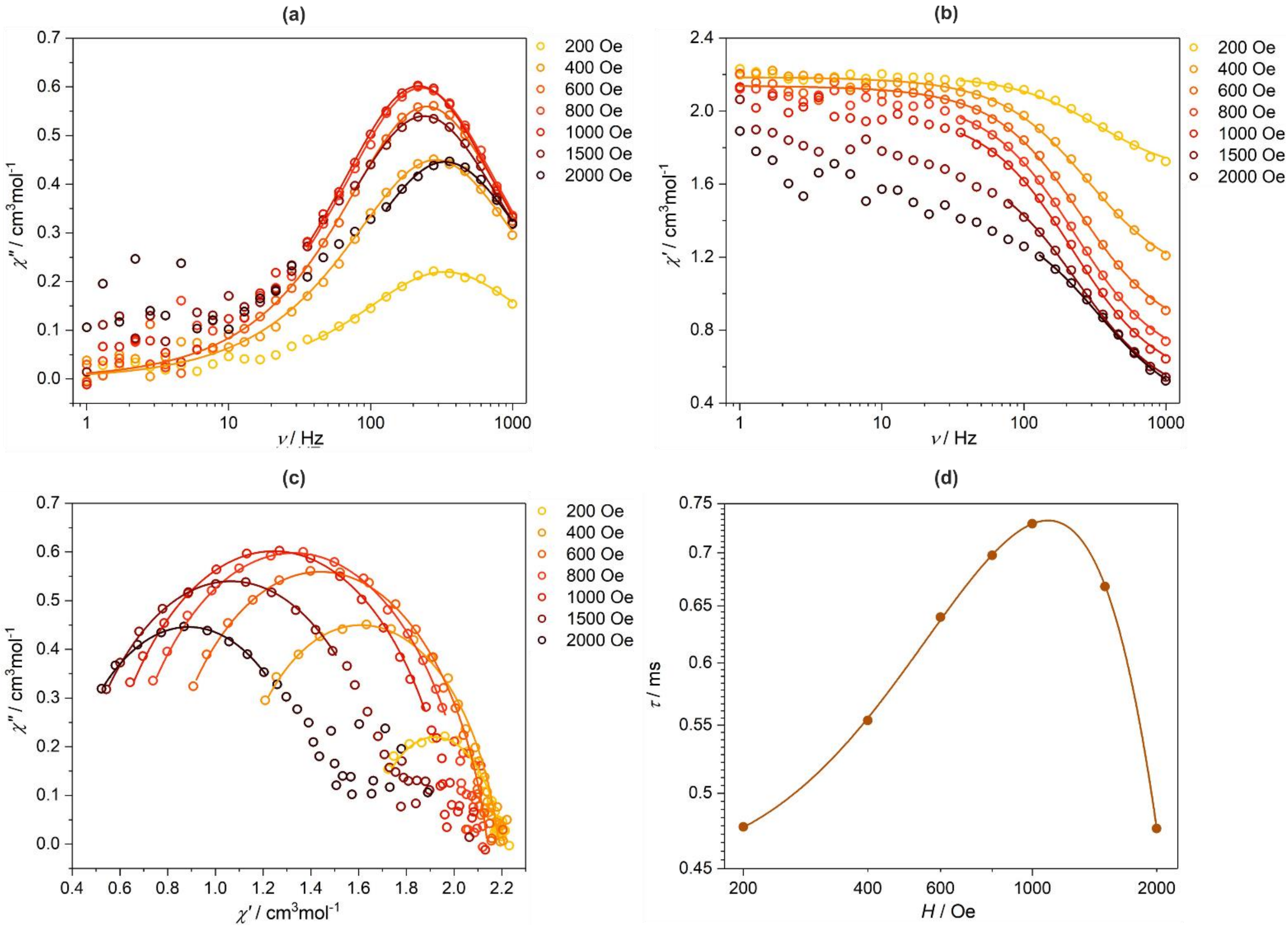

Figure S10. Complete magnetic-field-variable alternate-current (*ac*) magnetic susceptibility characteristics of **ErW** at T = 1.8 K, under H_{ac} = 1 Oe, and their analysis: frequency dependences of the out-of-phase susceptibility, χ'' (*a*), and the in-phase susceptibility, χ' (*b*) at various indicated *dc* external magnetic fields, together with the related Argand plots (*c*), and the field dependence of the relaxation time, τ (*d*). Both field and relaxation time were presented in (*d*) in the logarithmic scale. Coloured solid curves in (*a*), (*b*), and (*c*) represent the best fits following the generalized Debye model for a single relaxation process (see comment on Page S22). The solid line in (*d*) shows the best fit taking into account quantum tunnelling of magnetization and the direct process in the range of 200–2000 Oe. The τ versus H_{dc} dependence was fitted using the equation (I). The best-fit parameters were gathered in Table 2.

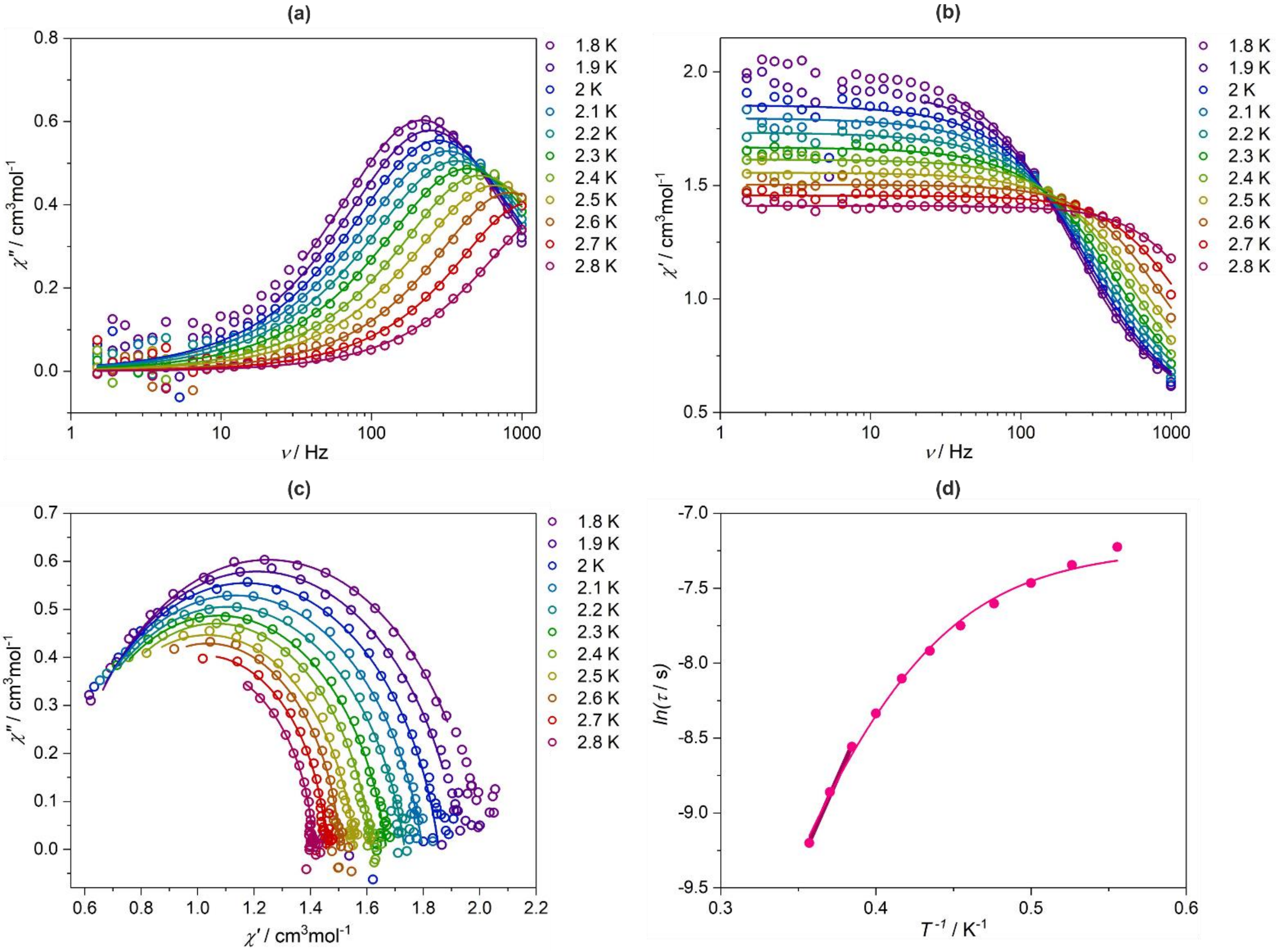

Figure S11. Complete temperature-variable alternate-current (*ac*) magnetic susceptibility characteristics of **ErW** under H_{ac} = 1 Oe, H_{dc} = 1000 Oe, and their analysis: frequency dependences of the out-of-phase susceptibility, χ'' (*a*), and the in-phase susceptibility, χ' (*b*) at various indicated temperatures, together with the related Argand plots (*c*), and the temperature dependence of the relaxation time, τ (*d*). Coloured solid curves in (*a*), (*b*), and (*c*) represent the best fits using the generalized Debye model for a single relaxation process (see comment on Page S22). The solid purple line in (*d*) represents the linear fitting following the Arrhenius law ($\ln\tau = \ln\tau_0 - (U_{eff}/k_B)\cdot T^{-1}$) in the range of 2.6–2.8 K. The best-fit parameters are U_{eff}/k_B = 24(1) K with $\tau_0 = 2.4(7)\cdot 10^{-8}$ s. The pink solid line in (*d*) shows the best fit of the full temperature-dependence of the relaxation time in the range of 1.8–2.8 K. The Orbach and Raman relaxation processes were taken into the account together with the direct process and quantum tunnelling of magnetization (QTM), both extracted from the field-dependence of the relaxation time. Therefore, we consequently followed the equation (II). The best-fit parameters were gathered in Table 2.

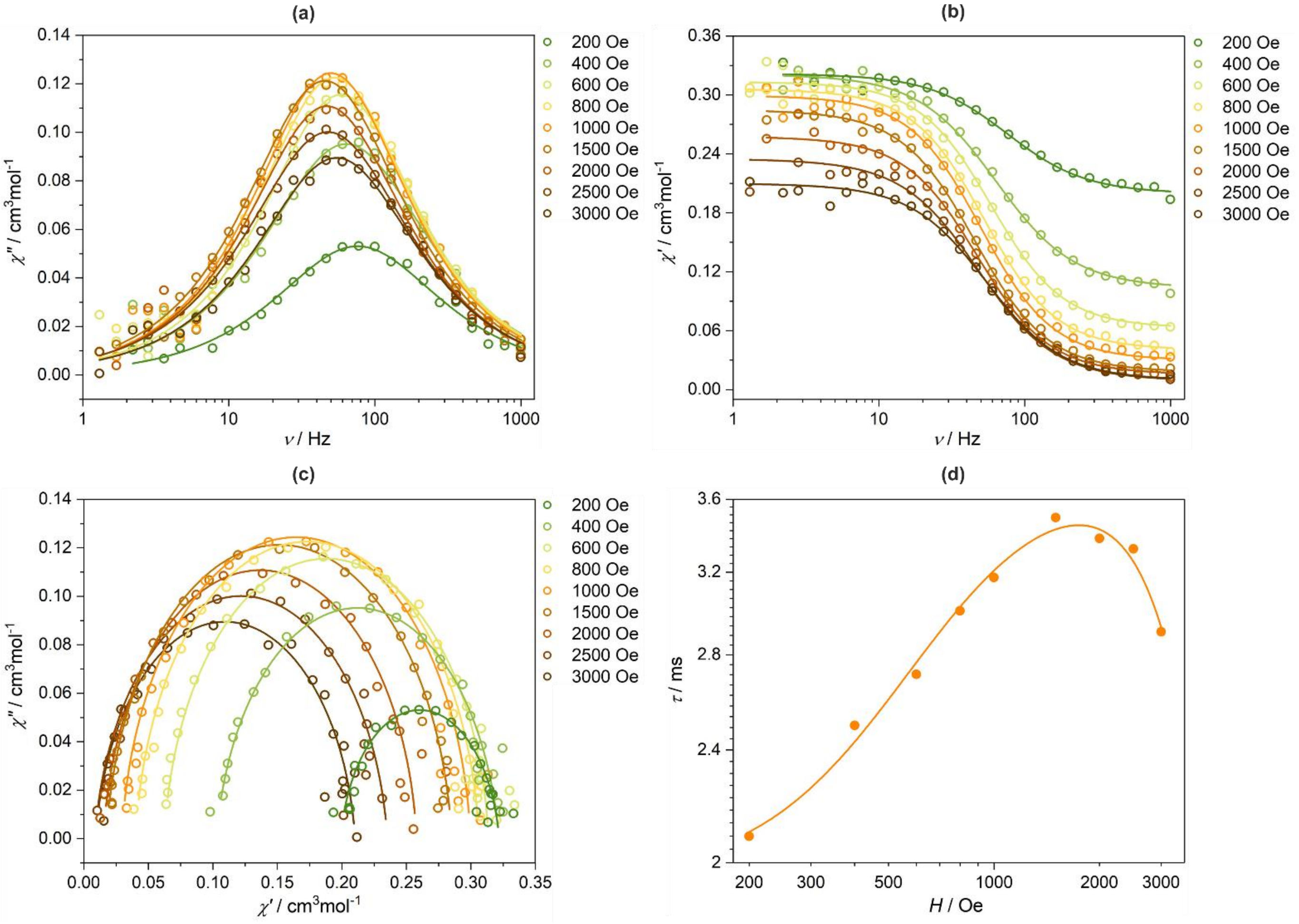

Figure S12. Complete magnetic-field-variable alternate-current (*ac*) magnetic susceptibility characteristics of **YbMo** at T = 1.8 K, under H_{ac} = 1 Oe, and their analysis: frequency dependences of the out-of-phase susceptibility, χ'' (*a*), and the in-phase susceptibility, χ' (*b*) at various indicated *dc* external magnetic fields, together with the related Argand plots (*c*), and the field dependence of the relaxation time, τ (*d*). Both field and relaxation time were presented in (*d*) in the logarithmic scale. Coloured solid curves in (*a*), (*b*), and (*c*) represent the best fits following the generalized Debye model for a single relaxation process (see comment on Page S22). The solid line in (*d*) shows the best fit taking into account quantum tunnelling of magnetization and the direct process in the range of 200–3000 Oe. The τ versus H_{dc} dependence was fitted using the equation (I) and the best-fit parameters were gathered in the Table 2.

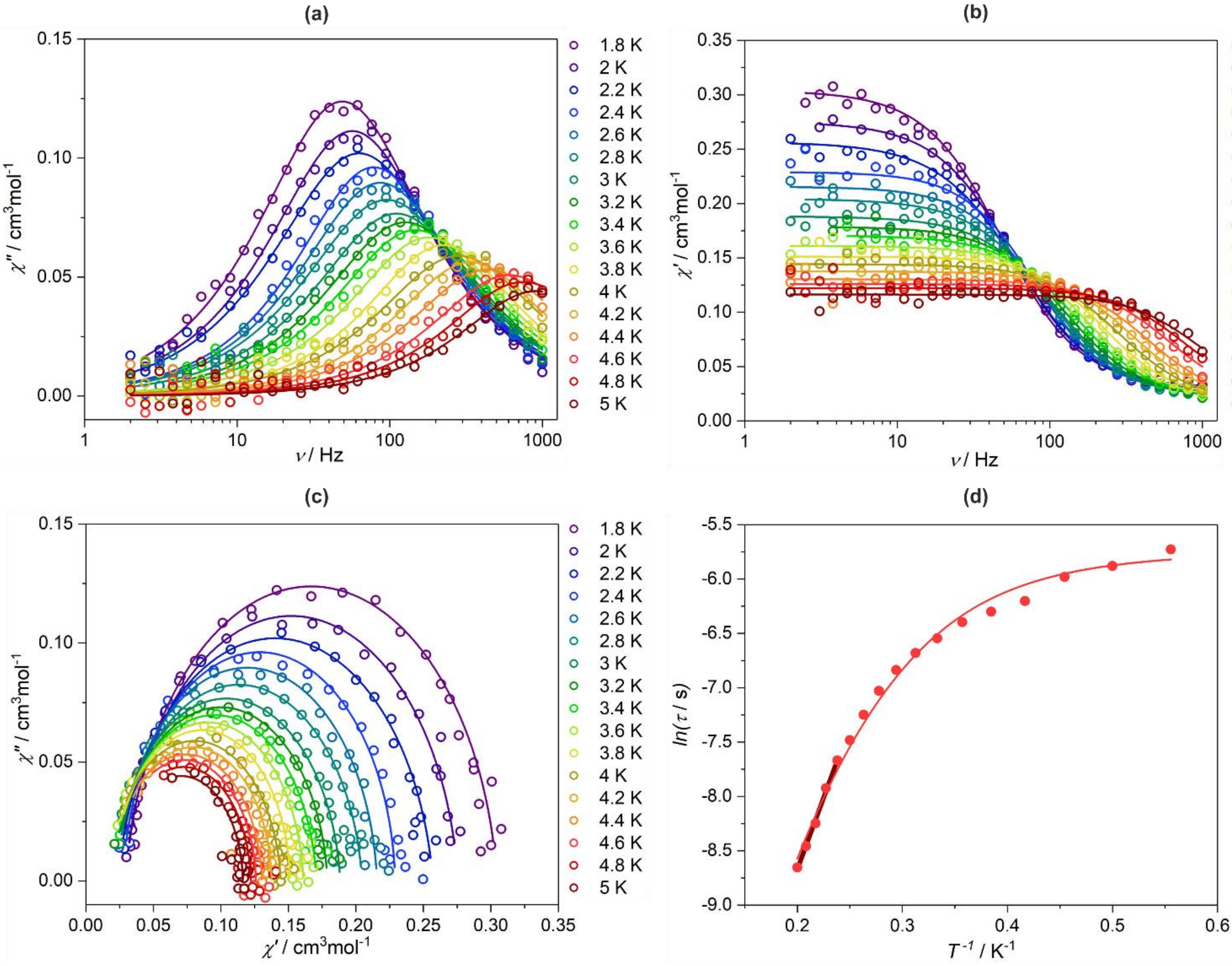

Figure S13. Complete temperature-variable alternate-current (*ac*) magnetic susceptibility characteristics of **YbMo** under H_{ac} = 1 Oe, H_{dc} = 1000 Oe, and their analysis: frequency dependences of the out-of-phase susceptibility, χ'' (*a*), and the in-phase susceptibility, χ' (*b*) at various indicated temperatures, together with the related Argand plots (*c*), and the temperature dependence of the relaxation time, τ (*d*). Coloured solid curves in (*a*), (*b*), and (*c*) represent the best fits using the generalized Debye model for a single relaxation process (see comment on Page S22). The solid deep red line in (*d*) represents the linear fitting following the Arrhenius law ($\ln\tau = \ln\tau_0 - (U_{\mathrm{eff}}/k_{\mathrm{B}})\cdot T^{-1}$) in the range of 4.2–5 K. The best-fit parameters are $U_{\mathrm{eff}}/k_{\mathrm{B}}$ = 26(1) K with τ_0 = 8.8(6)·10^{-7} s. The red solid line in (*d*) shows the best fit of the full temperature-dependence of the relaxation time in the range of 1.8–5 K. The Raman relaxation proces was taken into the account together with the direct process and quantum tunnelling of magnetization (QTM), both extracted from the field-dependence of the relaxation time. Therefore, we followed the equation (II) but without the Orbach relaxation which was found to be not necessary to reproduce the experimental data. The best-fit parameters were gathered in Table 2.

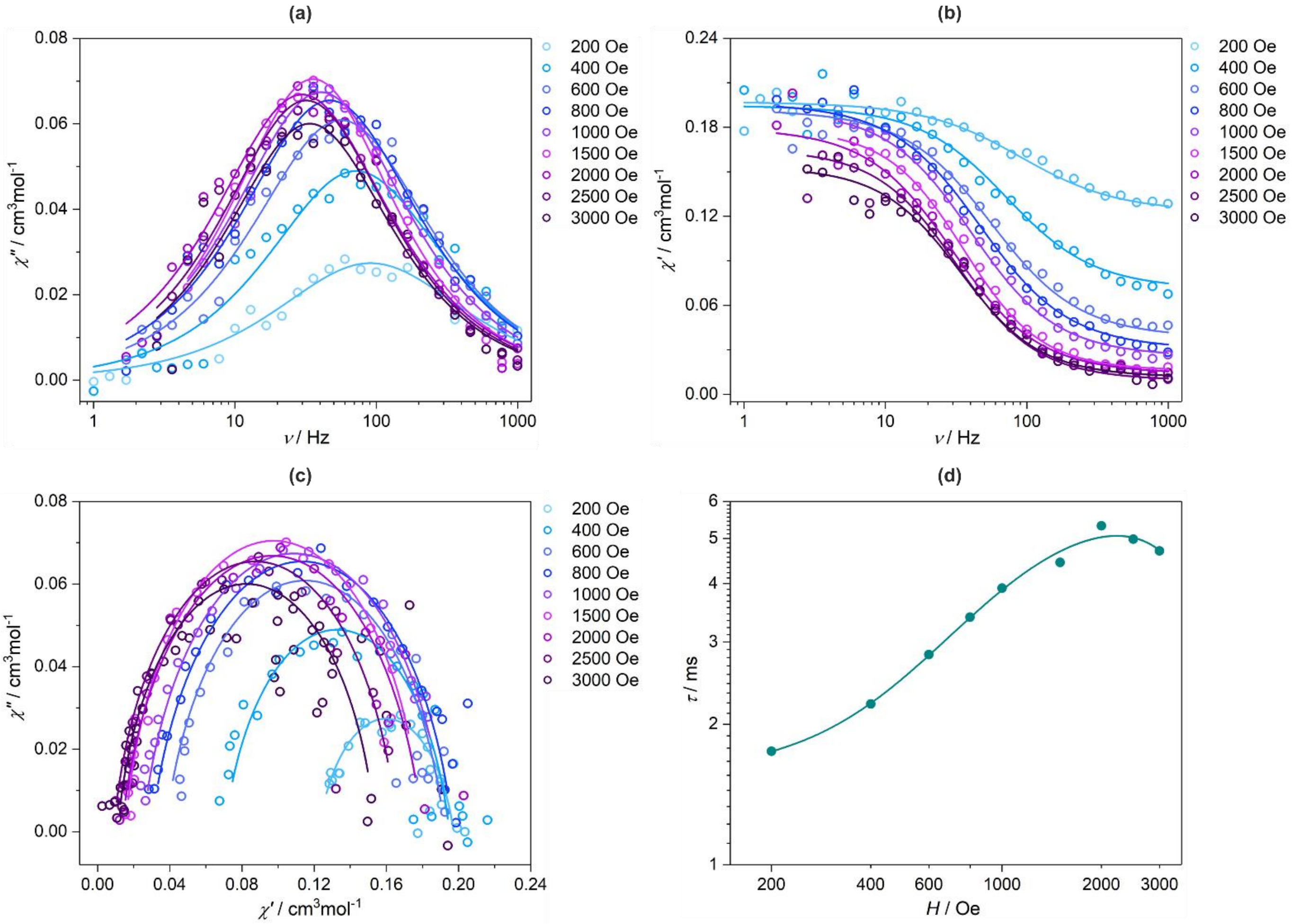

Figure S14. Complete magnetic-field-variable alternate-current (*ac*) magnetic susceptibility characteristics of **YbW** at T = 1.8 K, under H_{ac} = 1 Oe, and their analysis: frequency dependences of the out-of-phase susceptibility, χ'' (*a*), and the in-phase susceptibility, χ' (*b*) at various indicated *dc* external magnetic fields, together with the related Argand plots (*c*), and the field dependence of the relaxation time, τ (*d*). Both field and relaxation time were presented in (*d*) in the logarithmic scale. Coloured solid curves in (*a*), (*b*), and (*c*) represent the best fits following the generalized Debye model for a single relaxation process (see comment on Page S22). The solid line in (*d*) shows the best fit taking into account quantum tunnelling of magnetization and the direct process in the range of 200–3000 Oe. The τ versus H_{dc} dependence was fitted using the equation (I) and the best-fit parameters were gathered in Table 2.

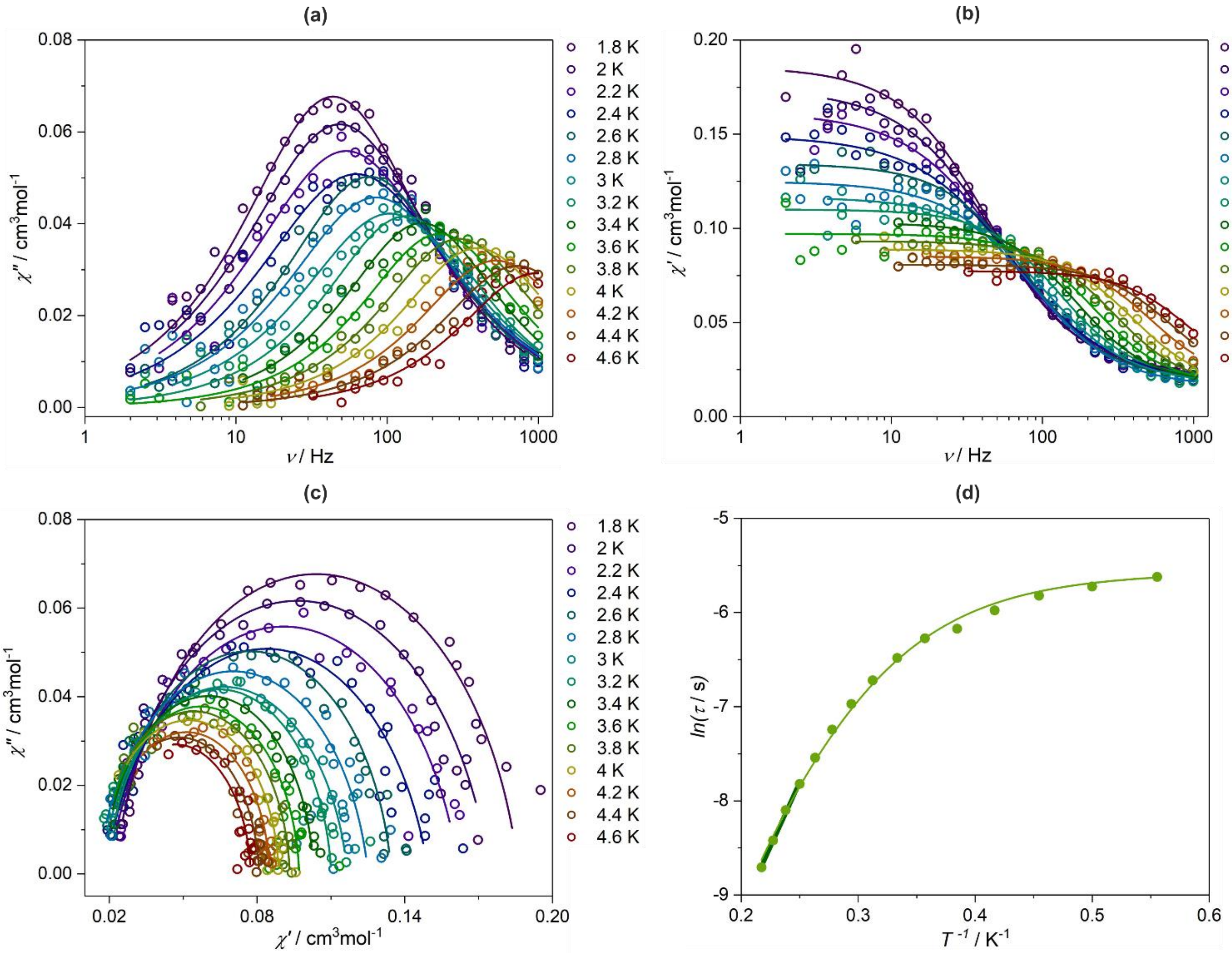

Figure S15. Complete temperature-variable alternate-current (*ac*) magnetic susceptibility characteristics of **YbW** under H_{ac} = 1 Oe, H_{dc} = 1000 Oe, and their analysis: frequency dependences of the out-of-phase susceptibility, χ'' (*a*), and the in-phase susceptibility, χ' (*b*) at various indicated temperatures, together with the related Argand plots (*c*), and the temperature dependence of the relaxation time, τ (*d*). Coloured solid curves in (*a*), (*b*), and (*c*) represent the best fits using the generalized Debye model for a single relaxation process (see comment on Page S22). The solid dark green line in (*d*) represents the linear fitting following the Arrhenius law ($\ln\tau = \ln\tau_0 - (U_{\mathrm{eff}}/k_{\mathrm{B}})\cdot T^{-1}$) in the range of 4–4.6 K. The best-fit parameters are $U_{\mathrm{eff}}/k_{\mathrm{B}}$ = 27(2) K with $\tau_0 = 4.6(9)\cdot10^{-7}$ s. The green solid line in (*d*) shows the best fit of the full temperature-dependence of the relaxation time in the range of 1.8–4.6 K. The Raman relaxation process was taken into the account together with the direct process and quantum tunnelling of magnetization (QTM), both extracted from the field-dependence of the relaxation time. Therefore, we followed the equation (II) but without the Orbach relaxation which was found to be not necessary to reproduce the experimental data. The best-fit parameters were gathered in Table 2.

Comment to Figures S8–S15

For the fitting of the frequency dependences of χ’ and χ” contributions to the *ac* magnetic susceptibility, and the related Argand χ”(χ’) plots in the case of double relaxation processes (Figure S8), the following equations (III and IV) of the generalized Debye model were used:

$$\chi'(\omega) = \chi_{S,total} + \Delta\chi_1 \frac{1+(\omega\tau_1)^{1-\alpha_1}\sin({}^{\pi\alpha_1}/_2)}{1+2(\omega\tau_1)^{1-\alpha_1}\sin({}^{\pi\alpha_1}/_2)+(\omega\tau_1)^{2(1-\alpha_1)}} + \Delta\chi_2 \frac{1+(\omega\tau_2)^{1-\alpha_2}\sin({}^{\pi\alpha_2}/_2)}{1+2(\omega\tau_2)^{1-\alpha_2}\sin({}^{\pi\alpha_2}/_2)+(\omega\tau_2)^{2(1-\alpha_2)}} \quad \text{(III)}$$

$$\chi''(\omega) = \Delta\chi_1 \frac{(\omega\tau_1)^{1-\alpha_1}\cos({}^{\pi\alpha_1}/_2)}{1+2(\omega\tau_1)^{1-\alpha_1}\sin({}^{\pi\alpha_1}/_2)+(\omega\tau_1)^{2(1-\alpha_1)}} + \Delta\chi_2 \frac{(\omega\tau_2)^{1-\alpha_2}\cos({}^{\pi\alpha_2}/_2)}{1+2(\omega\tau_2)^{1-\alpha_2}\sin({}^{\pi\alpha_2}/_2)+(\omega\tau_2)^{2(1-\alpha_2)}} \quad \text{(IV)}$$

where

$\chi_{\mathrm{S,total}}$ = the sum of the adiabatic susceptibilities of two separate relaxation processes ($\chi_{\mathrm{S,1}} + \chi_{\mathrm{S,2}}$),

$\Delta\chi_1$ = the difference between the adiabatic susceptibility ($\chi_{\mathrm{S,1}}$) and the isothermal susceptibility ($\chi_{\mathrm{T,1}}$) of the first relaxation process,

$\Delta\chi_2$ = the difference between the adiabatic susceptibility ($\chi_{\mathrm{S,2}}$) and the isothermal susceptibility ($\chi_{\mathrm{T,2}}$) of the second relaxation process,

τ_1 and τ_2 = the relaxation times of the first and the second relaxation processes, respectively,

α_1 and α_2 = the distribution (Cole-Cole) parameters of the first and the second relaxation processes, respectively, and ω is an angular frequency, that is $\omega = 2\pi v$, with v stands for the linear frequency in [Hz] units.

For the fitting of the frequency dependences of χ’ and χ” contributions to the *ac* magnetic susceptibility, and the related Argand χ”(χ’) plots in the case of single relaxation process (Figures S9–S15), the following equations (V and VI) of the generalized Debye model were applied:

$$\chi'(\omega) = \chi_S + (\chi_T - \chi_S)\frac{1+(\omega\tau)^{1-\alpha}\sin({}^{\pi\alpha}/_2)}{1+2(\omega\tau)^{1-\alpha}\sin({}^{\pi\alpha}/_2)+(\omega\tau)^{2(1-\alpha)}} \quad \text{(V)}$$

$$\chi''(\omega) = (\chi_T - \chi_S)\frac{(\omega\tau)^{1-\alpha}\cos({}^{\pi\alpha}/_2)}{1+2(\omega\tau)^{1-\alpha}\sin({}^{\pi\alpha}/_2)+(\omega\tau)^{2(1-\alpha)}} \quad \text{(VI)}$$

where

χ_{S} = the adiabatic susceptibility (at infinitely high frequency of *ac* field),

χ_{T} = the isothermal susceptibility (at infinitely low frequency of *ac* field),

τ = the relaxation time,

α = the distribution (Cole-Cole) parameter,

and ω is an angular frequency, that is $\omega = 2\pi v$, with v being for the linear frequency in [Hz] units.

In all fitting procedures, we firstly applied equations (III)/(IV) or (V)/(VI) to fit both χ’(ν) and χ”(ν) plots. After that, we obtained all important parameters including crucial relaxation times at each temperature and *dc* magnetic field. It was followed by checking the quality of the fittings by drawing the Argand (Cole-Cole) χ”(χ’) plots. For all compounds, the experimental χ’(ν) and χ”(ν) plots as well as the related Argand plots were reproduced nicely by the fitted curves (Figure S8–S15).

Reference: Y.-N. Guo, G.-F. Xu, Y. Guo and J. Tang, *Dalton Trans.*, 2011, **40**, 9956.

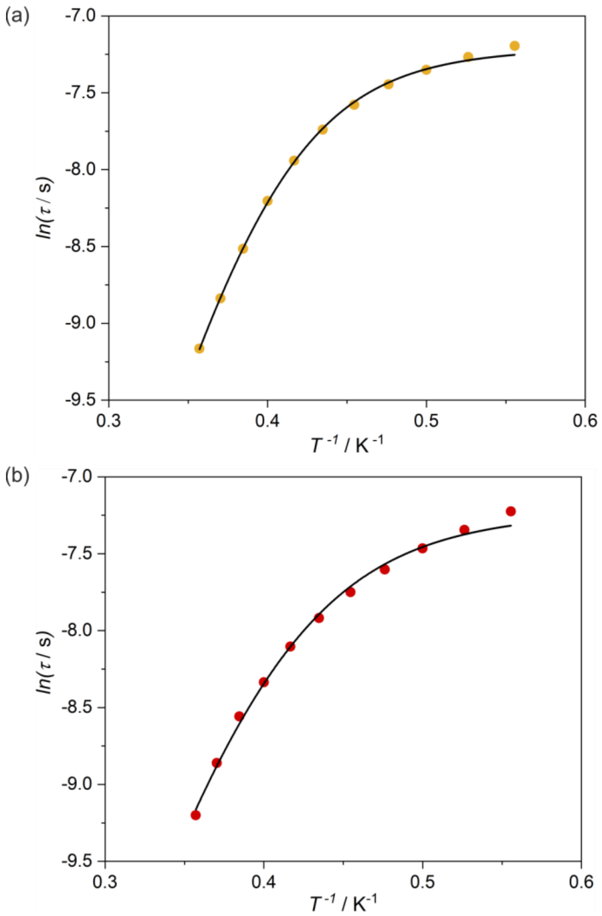

Figure S16. Alternative fitting of the temperature dependences of relaxation times in **ErMo** (*a*) and **ErW** (*b*) for the *ac* magnetic data gathered under H_{ac} = 1 Oe, H_{dc} = 600 Oe (**ErMo**, Fig. S9) or H_{dc} = 1000 Oe (**ErW**, Fig. S11). The fitting curves are related to the Equation (II) (Figure S9) but Orbach relaxation was excluded and the (*n*) power of Raman relaxation was not fixed. The obtained best-fit parameters are B_{Raman} = 0.086(2) $\mathrm{s^{-1}K^{-n}}$ with n = 11.1(2) for **ErMo** and B_{Raman} = 0.52(14) $\mathrm{s^{-1}K^{-n}}$ with n = 9.4(3) for **ErW**. The parameters of QTM effect and direct process were taken from the field-dependent a*c* data (Table 2).

Comment to Figure S16: The obtained fit without the Orbach relaxation and with free power (*n*) of Raman relaxation reasonably reproduce the experimental data (Fig. S9). However, the obtained powers of Raman T^{n} exceeded the typical range of 2–9. This effect was very rarely postulated in the literature (A. Kiel and W. B. Mims, *Phys. Rev.*, 1967, **386**, 161) and it was connected with a large difficulty in distinguishing of Raman process with such high powers of T^{n} from the exponential temperature dependence of an Orbach process. Moreover, the Raman *B* parameters were also found to be surprisingly very different for **ErMo** and **ErW**, rather not expected for such closely related structures. Therefore, we postulate that the Orbach process can be valid for Er-based analogues. We also tried to employ a phonon bottleneck effect instead of a typical direct process (P. L. Scott and C. D. Jeffries, *Phys. Rev.*, 1962, **127**, 32). This change with a fixed Raman process without an Orbach relaxation gave very poor fitting, so it was discarded. On the other hand, we also used a phonon bottleneck effect instead of a typical direct process for the case of free Raman power T^{n} without an Orbach relaxation. The reasonable fit could be obtained but it does not change significantly the high powers of T^{n}, well above the expected range of 2–9, giving the identical conclusion as mentioned above.

Table S8. Summary of the deconvolution performed for the solid-state UV-Vis absorption spectra of **ErMo**, **ErW**, **YbMo** and **YbW** (Figure 4).

Absorption band	**LnMo (Ln = Er, Yb)** Figures 4a, 4c	Absorption band	**LnW (Ln = Er, Yb)** Figures 4b, 4d
1	41000 cm^{-1} (ca. 245 nm)	I	39400 cm^{-1} (ca. 255 nm)
2	36480 cm^{-1} (ca. 275 nm)	II	35670 cm^{-1} (ca. 280 nm)
3	31800 cm^{-1} (ca. 315 nm)	III	31900 cm^{-1} (ca. 310 nm)
4	27000 cm^{-1} (ca. 370 nm)	IV	27200 cm^{-1} (ca. 365 nm)
5	23300 cm^{-1} (ca. 430 nm)	V	23000 cm^{-1} (ca. 435 nm)
6	19400 cm^{-1} (ca. 515 nm)	VI	17300 cm^{-1} (ca. 575 nm)

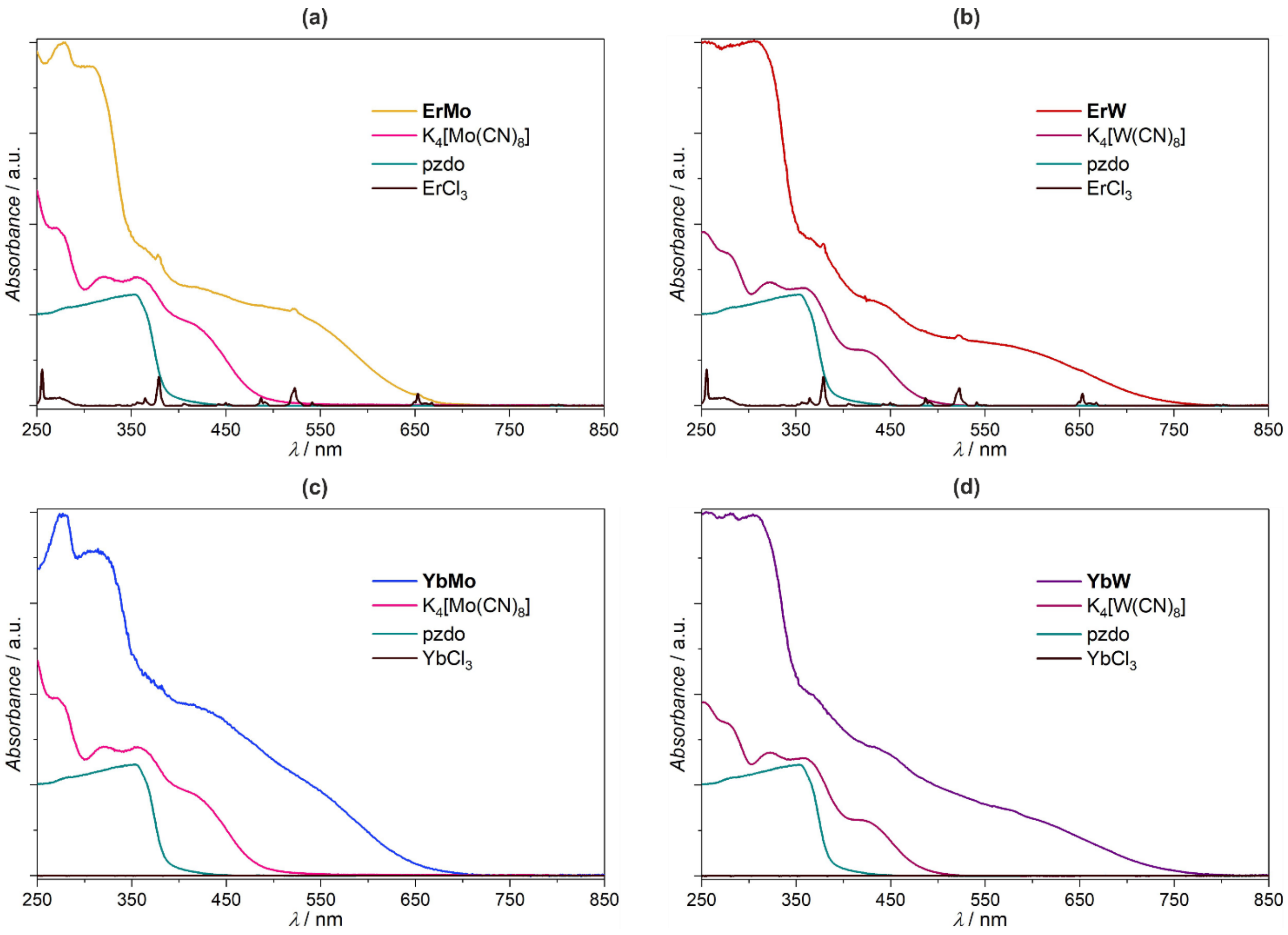

Figure S17. Solid-state UV-Vis absorption spectra of **ErMo** (*a*), **ErW** (*b*), **YbMo** (*c*) and **YbW** (*d*) compared with the reference spectra of the respective octacyanidometallate(IV) salts, organic ligand and the respective lanthanide(III) chlorides.

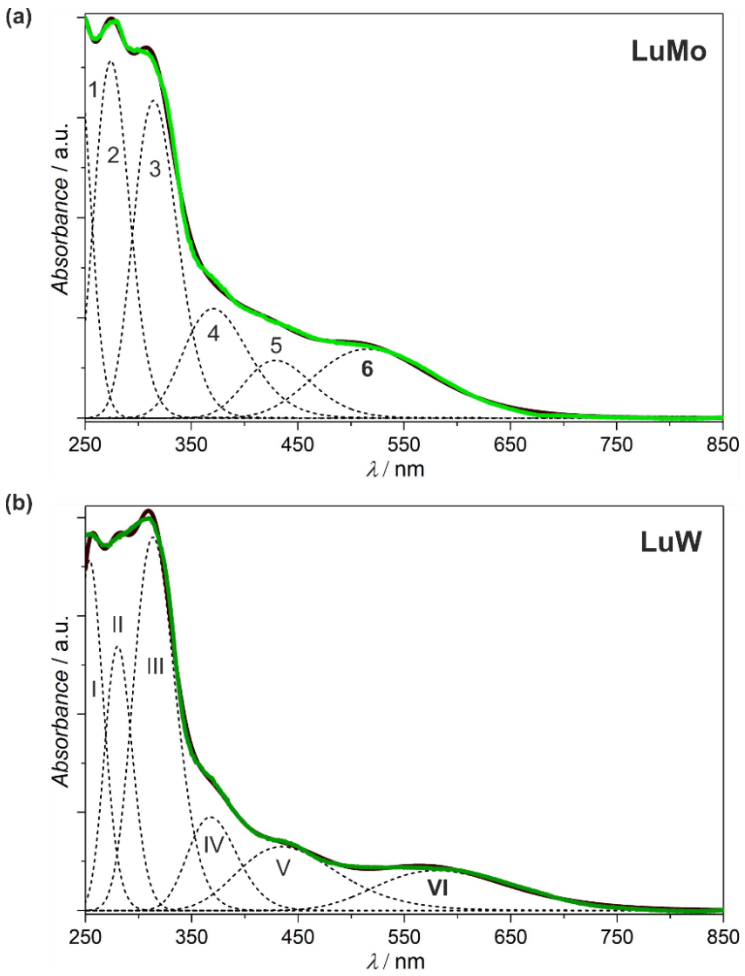

Figure S18. Solid-state UV-Vis absorption spectra of the lutetium(III) analogues, **LuMo** (*a*) and **LuW** (*b*), together with deconvolution of the absorption bands performed using parameters from Table S7.

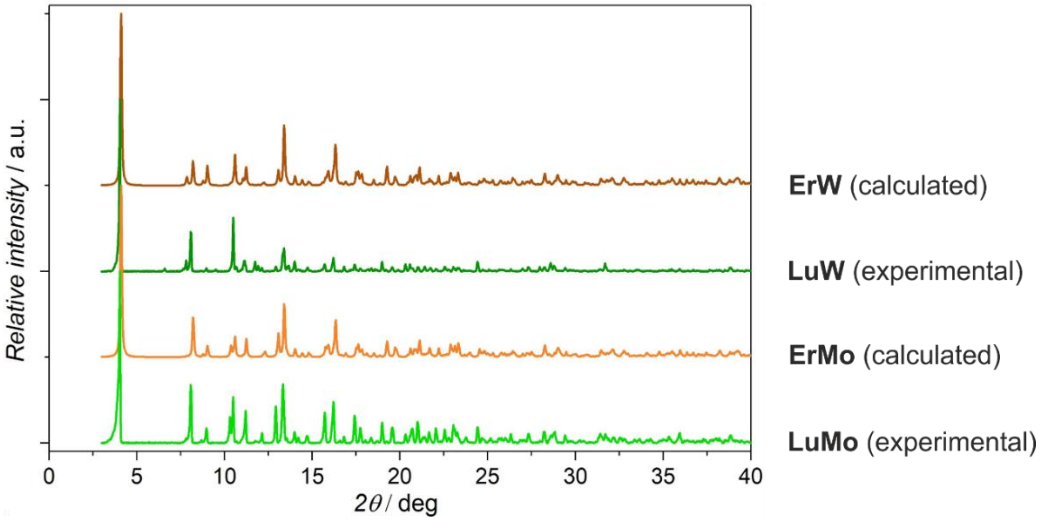

Figure S19. Experimental powder X-ray diffraction (PXRD) patterns of lutetium(III) analogues, **LuMo** and **LuW**. For comparison, the PXRD pattern calculated from the structural models of **ErMo** and **ErW** obtained within the single crystal X-ray diffraction structural analyses were also presented. The Lu(III)-containing compounds analogous to the ErMo, ErW, YbMo and YbW compounds described in the manuscript, were prepared following the identical synthetic procedures using the appropriate Lu(III) precursor. The isostructurality of the **LuMo** and **LuW** compounds was confirmed by the PXRD pattern shown above.

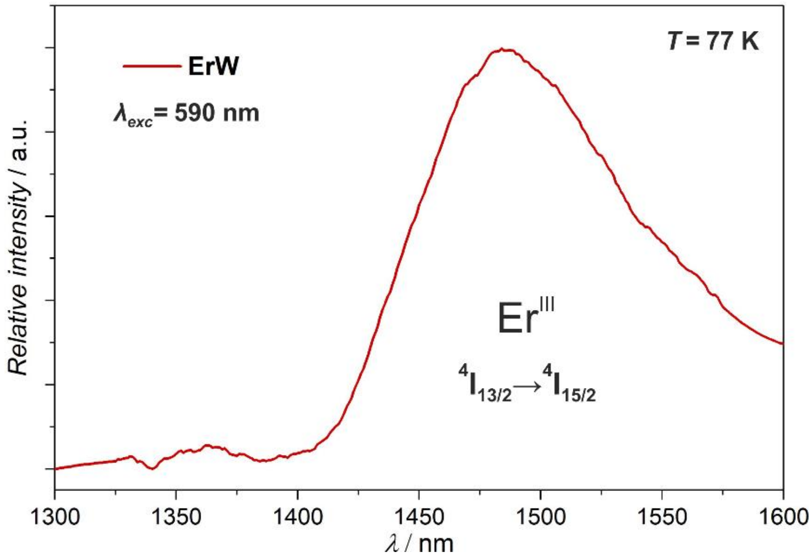

Figure S20. Solid-state emission spectra of **ErW** gathered at the temperature of 77 K in the range 1300–1600 nm using the indicated excitation wavelength of 590 nm.

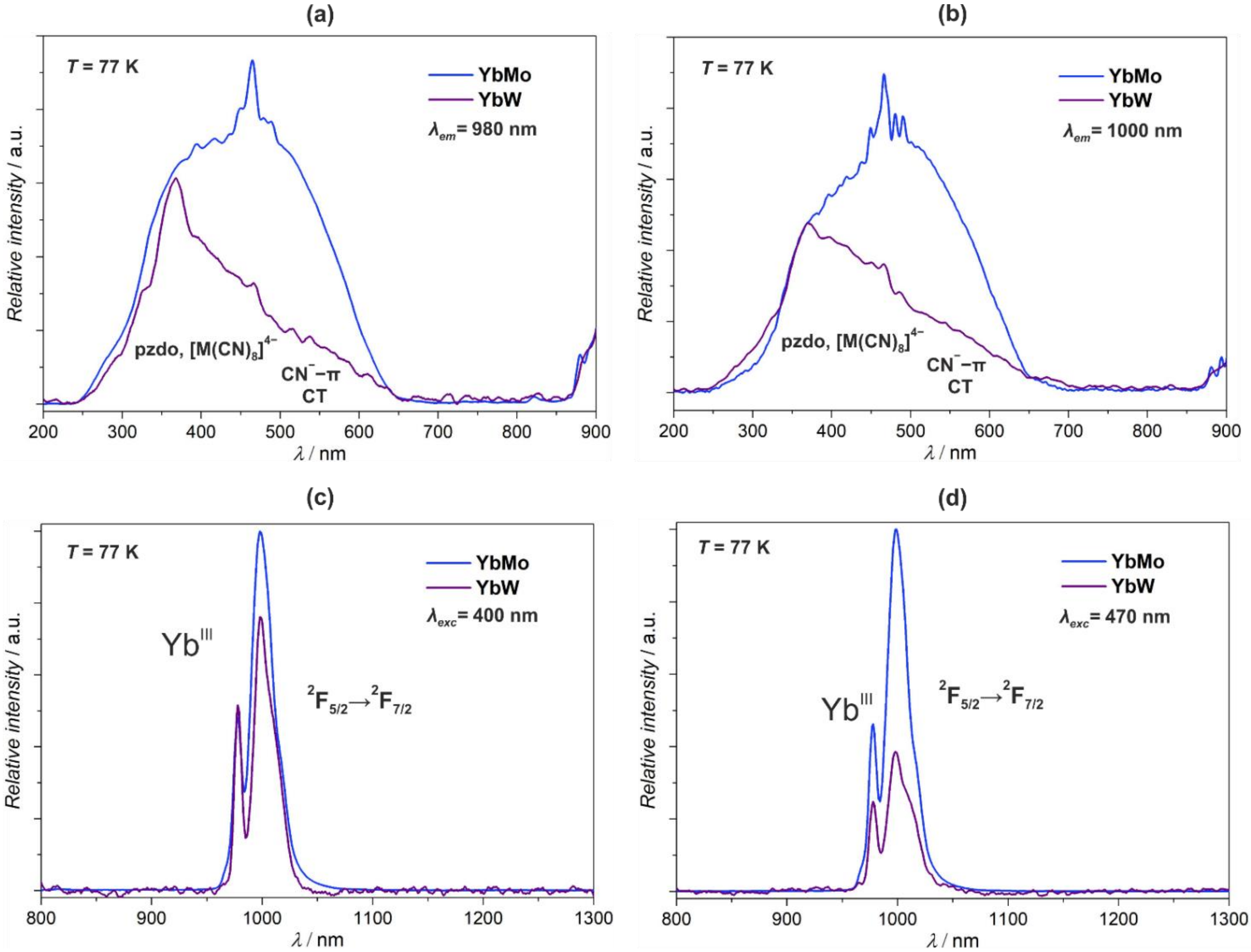

Figure S21. Solid-state excitation (*a*, *b*) and emission (*c*, *d*) spectra of **YbMo** and **YbW** gathered at the temperature of 77 K using the indicated emission and excitation wavelengths.

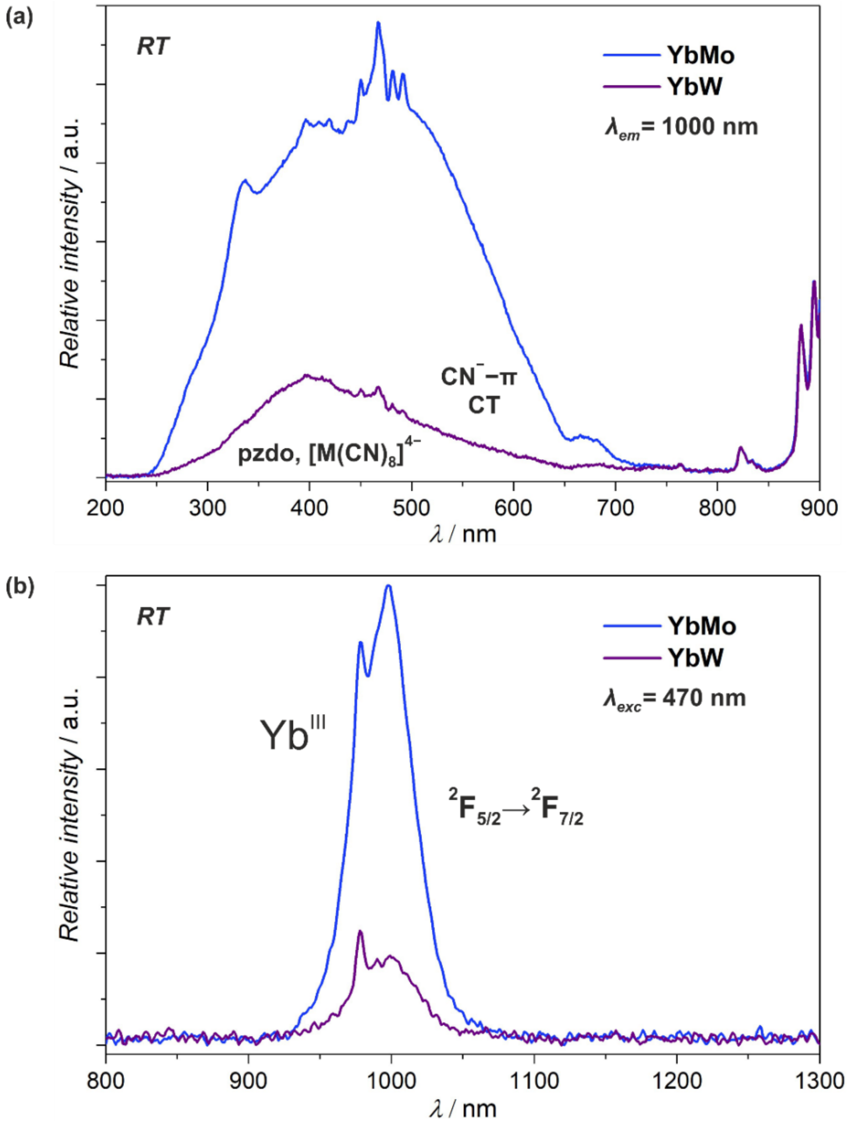

Figure S22. Additional solid-state excitation (*a*) and emission (*b*) spectra of **YbMo** and **YbW** gathered at room temperature using the indicated emission and excitation wavelengths.

Table S9. Crystal data and structure refinement for **YbMo-hyd** and **YbW-hyd**.

Compound		**YbMo-hyd**	**YbW-hyd**
formula		$Yb_2Mo_2C_{104.6}H_{86}N_{26}O_{34}P_4$	$Yb_2W_2C_{104.6}H_{86}N_{26}O_{34}P_4$
formula weight [g·mol^{-1}]		2913.03	3088.85
T [K]		100(2)	
λ [Å]		0.71073	
crystal system		monoclinic	
space group		$P\ 2_1/c$	
unit cell	***a*** [Å]	11.1351(11)	11.1462(13)
	b [Å]	13.0368(13)	13.0441(17)
	c [Å]	42.691(4)	42.861(5)
	β [deg]	93.430(2)	92.511(3)
V [Å^3]		6186.2(11)	6225.7(13)
Z		2	2
calculated density [g·cm^{-3}]		1.564	1.648
absorption coefficient [cm^{-1}]		1.833	3.467
F(000)		2903	2903
crystal size [mm × mm × mm]		0.28 × 0.13 × 0.10	0.28 × 0.13 × 0.04
crystal type		red block	black block
Θ range [deg]		2.568–26.731	2.581–25.027
limiting indices		$-14 < h < 14$ $-16 < k < 16$ $-54 < l < 54$	$-13 < h < 13$ $-15 < k < 14$ $-51 < l < 26$
collected reflections		59437	24611
unique reflections		13130	10592
R_{int}		0.0736	0.0979
completeness		0.999	0.993
max. and min. transmission		0.628 and 0.838	0.503 and 0.874
data/restraints/parameters		13130/188/796	24611/237/796
GOF on F^2		1.454	1.259
final R indices		$R_1 = 0.1210$ [$I > 2\sigma(I)$] $wR_2 = 0.2614$ (all data)	$R_1 = 0.1077$ [$I > 2\sigma(I)$] $wR_2 = 0.1874$ (all data)
largest diff peak/hole		4.442/-5.231 e·Å^{-3}	2.703/-3.973 e·Å^{-3}

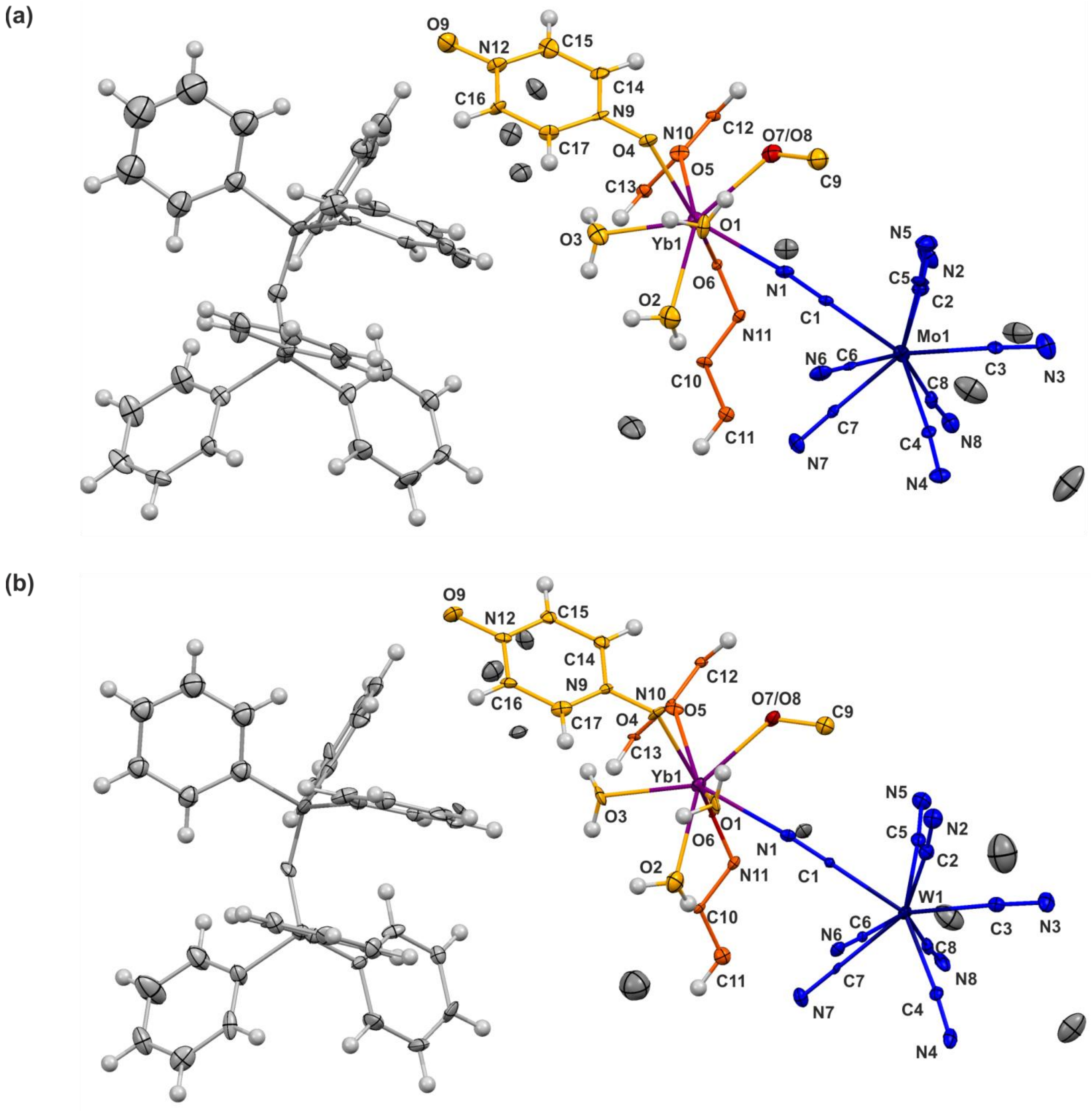

Figure S23. Comparison of the asymmetric units of **YbMo-hyd** (*a*) and **YbW-hyd** (*b*) with the atoms labelling schemes. Thermal ellipsoids are presented at the 50% probability level. Hydrogen atoms were drawn as fixed-sized spheres with the 0.2 Å radius.